

## Electronic Supporting Information

A highly elastic and Li-ion conductive binder enables stable operation of silicon microparticle anodes in high-capacity and high-energy-density pouch cells

Zheng Li,<sup>‡\*</sup> Zhengwei Wan,<sup>‡</sup> Zheng Lin, Mengting Zheng,<sup>\*</sup> Jianhui Zheng, Shangshu Qian, Yao Wang, Tinglu Song, Zhan Lin,<sup>\*</sup> and Jun Lu<sup>\*</sup>

Prof. Z. H. Li, Dr. Z. W. Wan, Dr. M. T. Zheng, Dr. J. H. Zheng, Dr. S. S. Qian, Prof. J. Lu

Zhejiang Provincial Key Laboratory of Advanced Chemical Engineering Manufacture Technology, College of Chemical and Biological Engineering, Zhejiang University, Hangzhou 310058, China

E-mail: zhengli@zju.edu.cn, mtzheng@zju.edu.cn, junzoelu@zju.edu.cn

Z. Lin, Prof. Z. Lin

School of Chemical Engineering and Light Industry, Guangdong University of Technology, Guangzhou 510006, China

E-mail: zhanlin@gdut.edu.cn

Prof. Y. Wang

College of Materials Science and Engineering, Zhejiang University of Technology, Hangzhou 310014, China.

Prof. T. L. Song

School of Materials Science and Engineering, Beijing Institute of Technology, Beijing 100081, China

## Experimental Section

**Materials.** Acrylic acid (AA) and Guar gum (GG) were purchased from Aladdin Reagent (Shanghai) Co., Ltd. Polyacrylic acid (PAA, 25 wt% in solution,  $M_w \approx 250,000$ ) was purchased from ACROS. Ammonium persulphate ( $(\text{NH}_4)_2\text{S}_2\text{O}_8$ ) and sodium hydrogen sulfite ( $\text{NaHSO}_3$ ) were obtained from Sinopharm Chemical Reagent Co., Ltd. Silicon nanoparticles (SiNPs,  $\sim 100$  nm) were purchased from Shanghai St-Nano Science and Technology Co., Ltd. Si microparticles (SiMPs,  $1\sim 5$   $\mu\text{m}$ ) was purchased from Alfa Aesar (China) Chemical Co., Ltd. Si submicroparticles (SiSMPs) were obtained by ball milling SiMPs. Typically, in a SiSMPs preparation process, zirconia grinding beads and SiMPs were mixed in a mass ratio of 20:1 and ball-milled for 20 h at  $400 \text{ r min}^{-1}$  under atmosphere to obtain SiSMP in a planetary ball mill machine (QM-3SP2, China). All reagents were used without further purification except for AA being used after the removal of 4-Methoxyphenol (MEHQ) as the polymerization inhibitor by rotary evaporation system (IKA RV10, German).

**Synthesis of GG-g-PAA.** 1 g of GG was dissolved in 99 g of deionized water in a 500 ml four-necked flask by vigorously magnetic stirring, purging with nitrogen gas for 24 h at room temperature. Then 0.1 g of  $(\text{NH}_4)_2\text{S}_2\text{O}_8$  and 0.03 g of  $\text{NaHSO}_3$  dissolved in 10 g of deionized water was slowly dropped into GG solution as the initiator, heated in a water bath after stirring for another 10 min. 15 g of AA was dropped into the above solution in a drip funnel when the bath reached  $60^\circ\text{C}$ , and then the reaction continued for 2.5 h under continuous stirring in a water bath of  $70^\circ\text{C}$ . The product was obtained after cooling to room temperature naturally, named as GG-g-PAA.

**Preparation of the SiMP electrodes.** To prepare the SiMP electrodes, SiMPs, super P conductive carbon (SP), and binder with a mass ratio of 8:1:1 were mixed in dispersant to form a homogeneous slurry. The slurry was then casted onto the current collector via a common doctor-blade coating method. After drying in a vacuum oven for 12 h at  $120^\circ\text{C}$ , the electrode film was cut into small disks with a diameter of 12 mm. Deionized water (DI)/ethanol mixture was used as dispersant for GG-g-PAA and PAA, and DI was used as dispersant for GG. The SiNP and SiSMPs electrodes with different binders were also prepared in the same process except that DI was used as dispersant for all

SiNP electrodes. Unless otherwise stated, the mass ratio of Si particles, SP and binder in SiNP and SiSMP electrodes is also 8:1:1.

**Cells Assembly.** To assemble coin-type half cells, the as-prepared electrodes were assembled into 2025-coin cells in an Ar-filled dry glove box containing less than 0.1 ppm of water and oxygen. For the half cells, the Li foil was used as the counter electrode and the Celgard 2325 membrane was used as the separator. 1.2 mol L<sup>-1</sup> lithium hexafluorophosphate (LiPF<sub>6</sub>) in a binary solvent of diethyl carbonate (DEC) and ethylene carbonate (EC) (1:1 in volume) containing 25 vol% fluoroethylene carbonate (FEC) was used as electrolyte, unless specified otherwise. To assemble coin-type full cells, LiNi<sub>0.8</sub>Co<sub>0.1</sub>Mn<sub>0.1</sub>O<sub>2</sub> (NCM811, areal mass loading of electrode film: 21.5 mg cm<sup>-2</sup>; mass percent of active material: 94.5%) electrode purchased from Canrd Co., Ltd. were used as the cathode, and the SiMP@GG-g-PAA electrode was used as the anode. The electrolyte of full cells contained 1.2 mol L<sup>-1</sup> LiPF<sub>6</sub> in a binary solvent of DEC and EC (1:1 in volume) with 10 vol% FEC and 1 wt% vinylene carbonate (VC). The n/p ratio defined by the areal capacity ratio between the anode and cathode was ≈1.1. For all coin-type half and full cells, 100 μL of electrolyte was injected.

To assemble pouch full cells based on SiMP@GG-g-PAA anode, NCM811 cathodes with different mass loadings (areal mass loading of electrode film (double sides): 43 or 55.6 mg cm<sup>-2</sup>; mass percent of active material: 94.5%) were purchased from Canrd Co., Ltd. The LiNi<sub>0.5</sub>Co<sub>0.2</sub>Mn<sub>0.3</sub>O<sub>2</sub> (NCM523) and Li-rich cathodes were fabricated by slurry consisting of NCM523 (Li-rich), super P, carbon nanotube (CNT), and polyvinylidene fluoride (PVDF) in a weight ratio of 94:2:2:2 in N-methyl-2-pyrrolidone. The slurry was cast onto aluminum foil and dried under vacuum. The n/p ratio defined by the capacity ratio between the anode and cathode was 1.1. The electrolyte of pouch full cells was 1 mol L<sup>-1</sup> LiPF<sub>6</sub> in a binary solvent of DEC and EC (1:1 in volume) with 20 wt% FEC and 1 wt% VC. 6.0 mL of electrolyte was injected into the 20-layer and 25-layer high-capacity NCM811/SiMP@GG-g-PAA pouch full cells, while 3.0 mL of electrolyte was injected into the other 0.5 and 1.0 Ah pouch full cells. The 2.4 Ah, 3.0 Ah, and 3.6 Ah Li-rich/SiMP@GG-g-PAA pouch full cells were injected with 5.0, 5.5, and 6.0 mL of a special electrolyte (LP75) for the Li-rich cathode, respectively.

**Electrochemical Test.** To evaluate electrochemical performance of coin-type half cells, a galvanostatic charge-discharge cycling test was carried out using LAND battery cycler (China) between 0.005 and 1.2 V. The half cells with all-type Si electrodes were activated at 0.03 C (1 C = 4200 mA g<sup>-1</sup>) for three cycles before the subsequent cycles. Cyclic voltammetry (CV) measurements of the SiMP electrode or binder films were recorded on an electrochemical work station (Solartron 1470E) between 0.005 and 1.2 V. Before the scan rate-dependent CV measurements, all SiMP electrodes were activated at 0.03 C for five cycles. EIS of the SiMP electrodes or binder films were recorded by a CHI660E electrochemical workstation with amplitude of 5 mV in the frequency range of 0.01 Hz-100 kHz. The galvanostatic intermittent titration technique (GITT) results were collected on a LAND battery cycler (China) between 0.005 and 1.2 V with a constant current pulse of 0.05 C for 10 min, followed by a relaxation time for 30 min, before all SiMP electrodes were activated at 0.03 C for five cycles before GITT measurements.

The Randles–Sevcik equation is used to analyze the Li ion diffusion ability of the different electrodes:<sup>1</sup>

$$I_p = 2.69 \times 10^5 n^{1.5} A D_{Li^+}^{0.5} \nu^{0.5} C_{Li^+} \quad (1)$$

where  $I_p$  indicates the peak current,  $C_{Li^+}$  is the Li-ion concentration in the electrolyte,  $A$  is the electrode area,  $\nu$  is the scanning rate (V s<sup>-1</sup>),  $n$  is the number of electrons in the reaction, and  $D_{Li^+}$  is the Li-ion diffusion coefficient (cm<sup>2</sup> s<sup>-1</sup>). It can be found that the slop of the linear relationship between  $I_p$  and  $\nu^{0.5}$  is positively correlated with  $D_{Li^+}$ .

The ionic conductivity of the electrolytes was measured by stainless-steel symmetrical cells. Ionic conductivity was calculated based on equation:<sup>2</sup>

$$\sigma = \frac{L}{R \times S} \quad (2)$$

where  $\sigma$  is the ionic conductivity,  $R$  is the bulk resistance,  $L$  is the thickness of the binder film, and  $S$  is the surface area of the stainless-steel spacer. All the potentials presented in this study were quoted versus Li/Li<sup>+</sup>.

The  $D_{Li^+}$  during discharging and charging states was calculated according to the

following equation:<sup>3</sup>

$$D_{Li^+} = \frac{4}{\pi\tau} \left( \frac{n_M V_M}{S} \right)^2 \left( \frac{\Delta E_S}{\Delta E_\tau} \right)^2 \quad (3)$$

where  $\tau$  is the pulse time,  $n_M$  is the number of moles,  $V_M$  is the molar volume of SiMPs,  $S$  is the electrode area,  $\Delta E_S$  is the potential change at the end of two subsequent relaxation periods,  $\Delta E_\tau$  is the potential change during the current pulse.

As for the coin-type full cells, in the initial three activation cycles of the full-cell measurements, the cells were charged at 0.03 C (1 C = 188 mA g<sup>-1</sup>) under CCCV mode with the cut-off current in the CV period being 0.003 C and discharged at 0.03 C under CC mode. In the subsequent cycles, the cells were charged at 0.2 C under CCCV mode with the cut-off current in the CV period being 0.02 C and discharged at 0.2 C under CC mode. Pouch full cells were carried out on a LAND battery testing system. Pouch full cells based on NCM523 and NCM811 cathodes were cycled a voltage window of 2.75–4.3 V. In the initial five activation cycles, the full cells were charged at 0.1 C (0.05 C for NCM811/SiMP@GG-g-PAA pouch cells) under CCCV mode with cut-off current in the CV period being 0.01 C (0.005 C for NCM811/SiMP@GG-g-PAA pouch cells) and discharged at 0.1 C (0.05 C for NCM811/SiMP@GG-g-PAA pouch cells) under CC mode. In the subsequent cycles, the cells were charged at 0.2 C (0.1 C for NCM811/SiMP@GG-g-PAA pouch cells) under CCCV mode with the cut-off current in the CV period being 0.02 C (0.01 C for NCM811/SiMP@GG-g-PAA pouch cells) and discharged at 0.2C (0.01 C for NCM811/SiMP@GG-g-PAA pouch cells) under CC mode. 1 C = 160 mA g<sub>NCM523</sub><sup>-1</sup> and 180 mA g<sub>NCM811</sub><sup>-1</sup>. Pouch full cells based on Li-rich cathodes were cycled a voltage window of 2.0–4.6 V. In the initial two activation cycles, the full cells were charged and discharged at 0.05 C (1 C = 200 mA g<sup>-1</sup>) under CC mode. In the subsequent cycles, the cells were charged at 0.1 C under CCCV mode and discharged at 0.1 C under CC mode. All tests were performed at room temperature.

**Materials Characterization.** Scanning electron microscopy (SEM) images were acquired using a field emission SEM (Zeiss Utral 55). Cross-sectional focused ion-

beam-SEM (FIB-SEM) images were acquired using a crossbeam instrument (Zeiss Auriga 40) equipped with a gallium FIB and a field emission SEM. In-situ thickness monitoring of pouch cells was conducted using an in-situ electrochemical dilatometry instrument (CBS1400, IEST). Fourier-transform infrared spectrometry (FTIR) spectra were recorded on a FTIR spectrophotometer (Nicolet 5700) in the range of 4000–400  $\text{cm}^{-1}$  using KBr pellets to characterize the interactions of the binders and Si@binder electrodes. X-ray diffractions (XRD) patterns were recorded on a Rigaku D/MAX-2550-PC X-ray diffractometer with Cu  $K\alpha$  radiation ( $\lambda = 0.154 \text{ nm}$ ) at room temperature. X-ray photoelectron spectroscopy (XPS) was acquired using an ESCALAB-250Xi X-ray photoelectron spectrometer (Thermo Scientific K-Alpha, USA) operating at an Al  $K\alpha$  radiation source. The 3D tomography of SEI on SiMP anode was collected by a time-of-flight secondary ion mass spectrometry (TOF-SIMS, PHI nano TOF II, ULVAC-PHI). A special transfer vessel, which can directly transfer the sample from the glovebox to the vacuum chamber of TOF-SIMS, was used during sample transfer without being exposed to ambient air. The sputter etching was performed using an  $\text{Ar}^+$  beam (3 kV 100 nA) to obtain a depth profile. The area of analysis is  $50 \mu\text{m} \times 50 \mu\text{m}$ , while the sputtering area is  $400 \mu\text{m} \times 400 \mu\text{m}$ . The rheology experiment was performed at  $25^\circ\text{C}$  by the rotary rheometer (HAAKE, RS6000) to identify the shear viscosity of these binder solution (2 wt%) at different shear rates (from 1 to  $300 \text{ s}^{-1}$ ). Differential electrochemical mass spectrometry (DEMS, QMG220M, Linglu) system was used to analyze the  $\text{CO}_2$  gas evolution of electrodes. Nanoindentation was conducted using an Agilent U9820A Nano Indenter G200. The  $180^\circ$  peeling test and binder tensile experiments were both performed under ambient atmospheric conditions at a fixed strain rate through Universal material testing machine (Zwick/Roell Z020). Before the peeling test, different electrode pieces were cut into  $20 \text{ mm} \times 10 \text{ mm}$ , and 3M transparent tape was affixed and rolled 3 times to ensure even adhesion. Binder films were prepared by drying binder aqueous solutions on a Teflon film at  $80^\circ\text{C}$  in a vacuum oven for 24 h. The dry binder films were cut into the same size as the electrode pieces used for peeling test. The dry binder films were soaked with the EC/DEC (1:1 in volume) mixture for 24 h before the tensile experiments. Atomic

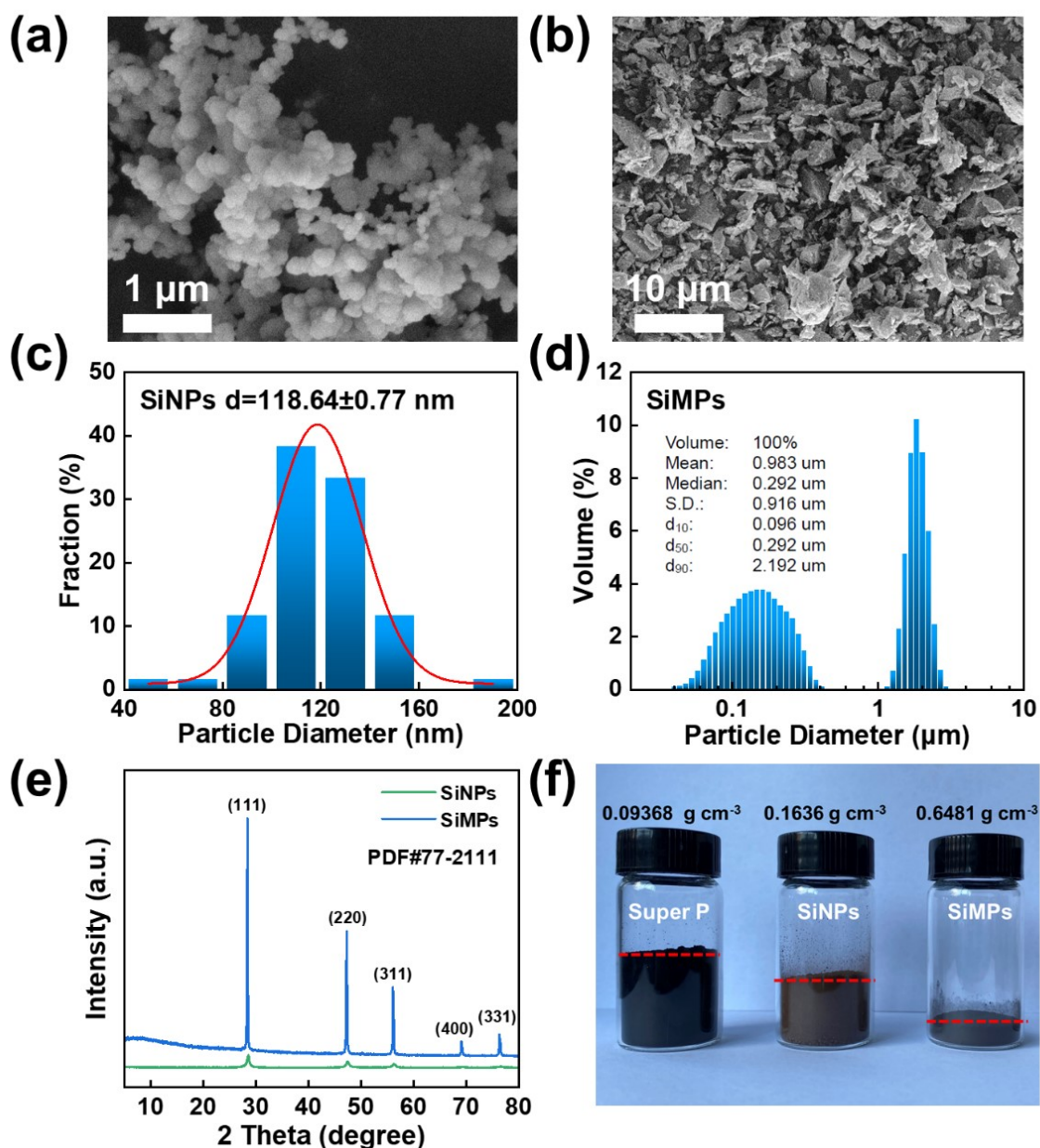
Force Microscopy (AFM) instrument (NT-MDT) was used to measure the adhesion force of different binder and observe the surface morphology of the electrodes. The contact angle of the binder to SiMP films were tested by the video-based optical contact angle measuring instrument (OCA 20, Dataphysics, German). Nuclear Magnetic Resonance ( $^1\text{H}$  NMR, Bruker 400MHz, German) test was performed to identify the chemical structure of PAA, GG and GG-g-PAA binder. Tap density test of super P, SiNPs, SiMPs, and SiSMPs was carried through vibration density tester (BT-313, China). Nitrogen adsorption-desorption specific surface area test was carried through high performance multi-channel automatic surface and pore analyzer (TriStar II Plus, USA) based on Brunner-Emmet-Teller (BET) measurements. Peak Force QNM mapping AFM (Dimension Icon, Bruker) experiments were performed to measure the adhesion, Young's modulus, and energy dissipation. The Young's modulus of different electrodes was fitting by the Derjaguin–Muller–Toporov model. The particle diameter distribution results of SiMPs and SiSMPs were obtained on a laser particle size analyzer (Beckman Coulter LS13320). The particle diameter distribution result of SiNPs was obtained through Nano Measurer software.

### **Computational Methods**

All the calculations were performed using the Vienna Ab initio Simulation Package (VASP).<sup>4</sup> The electron exchange–correlation interactions were described by the Perdew–Burke–Ernzerhof (PBE) parameterization within the generalized gradient approximation (GGA) approximation.<sup>5</sup> The size of the silicon slab is  $13.30 \times 11.52 \times 33.00$  Å, and the dangling bond on the silicon surface are saturated with hydroxyl groups. The projected augmented wave (PAW)<sup>6, 7</sup> pseudopotentials were employed to represent the electron-ion interactions with a cutoff energy of 500 eV and  $3 \times 3 \times 1$  k-point mesh were used for the slab. The force convergence criterion is  $0.02$  eV/Å for all the geometry optimized calculations. In order to avoid the effect of periodicity,  $15$  Å of vacuum was added along the z axis. VESTA<sup>8</sup> is used to visualize the atomic configurations. DFT-D3 method was used to describe van der Waals interactions.<sup>9</sup> The adhesion energy  $E_{\text{ad}}$  is defined as:

$$E_{\text{ab}} = E_{\text{tot}} - E_{\text{Silab}} - E_{\text{p}} \quad (4)$$

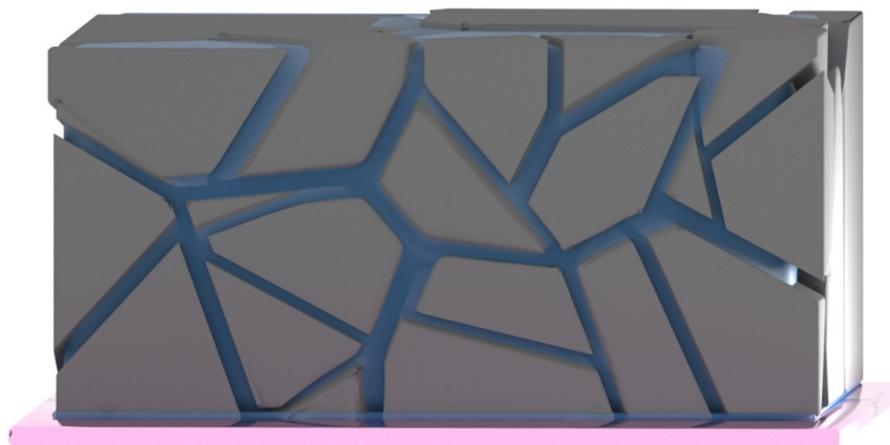
$E_{\text{tot}}$  represents the total energy of adsorbed structure composed by polymer fragments and silicon slab.  $E_{\text{p}}$  and  $E_{\text{Silab}}$  represent the energies of them, respectively.



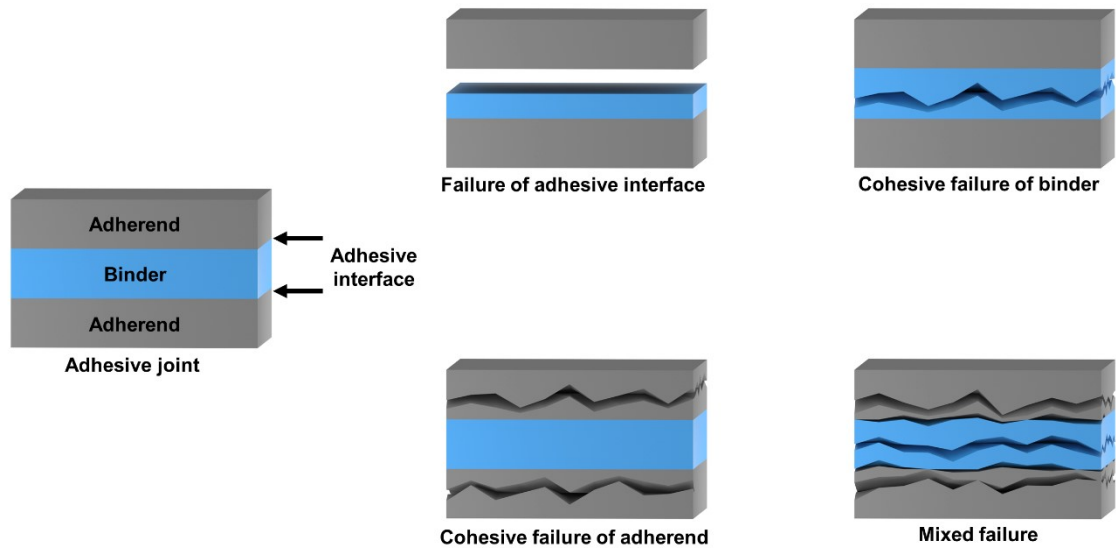
**Fig. S1** (a and b) SEM images of (a) SiNPs and (b) SiMPs. (c and d) Size distribution of (a) SiNPs and (b) SiMPs. (e) XRD patterns of SiNPs and SiMPs. (f) Photograph of SP, SiNPs and SiMPs with the same weight (1 g) and their corresponding tap densities.

As shown in Fig. S1a and S1c, the particle size of SiNPs is mainly distributed between 90 to 150 nm with only 1.7% of particles exceeding the critical breaking size (CBS) of 150 nm,<sup>10, 11</sup> suggesting that the SiNP anodes only undergoes volume expansion and contraction during the lithiation/delithiation process, with minimal particle pulverization occurring. In contrast, SiMPs exhibit a majority of particles exceeding the

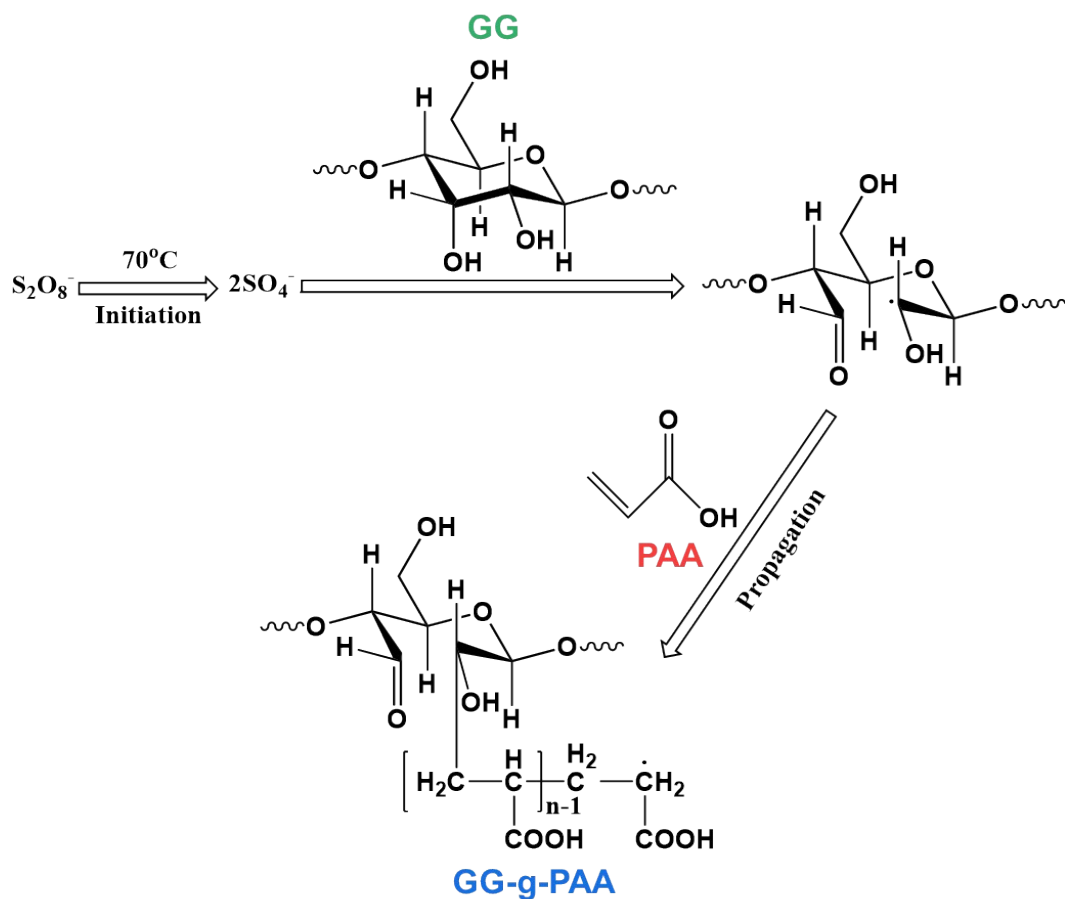
CBS, indicating that severe particle pulverization occurs of the SiMP anodes during the during the lithiation/delithiation process (Fig. S1b and S1d). Despite this, it is noteworthy that the tap density of SiMPs is four times higher than that of SiNPs (Fig. S1f), so the introduction of SiMP anodes can significantly increase the volumetric energy density of the lithium-ion batteries (LIBs). Consequently, the crucial task of addressing the challenge of additional adherend failure resulting from the pulverization of SiMPs arises, particularly in the development of SiMP anodes-based LIBs characterized by both high-gravimetric and high volumetric energy density.



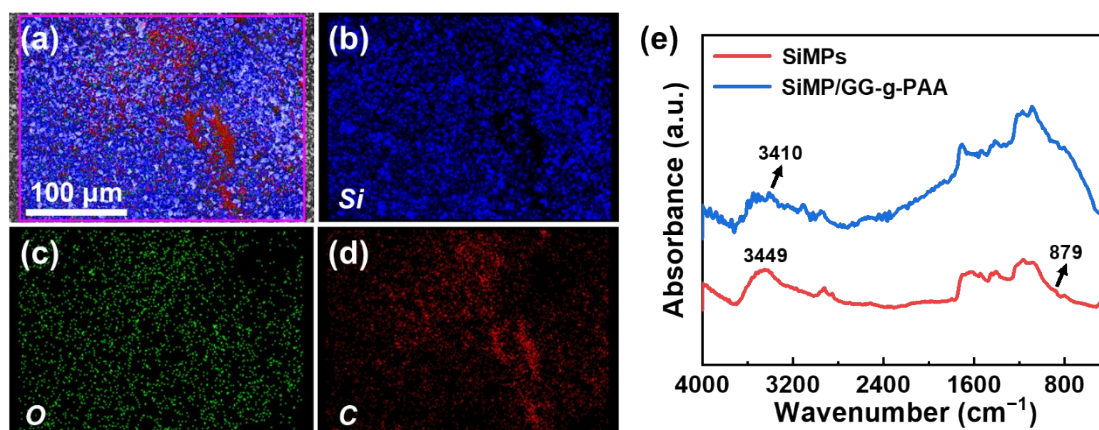
**Fig. S2** Schematic illustration of SiMPs-binder adhesive joints in the SiMP anode.



**Fig. S3** Schematic illustration of failure modes of the adhesive joint: failure of adhesive interface, cohesive failure of binder, cohesive failure of adherend, and mixed failure.

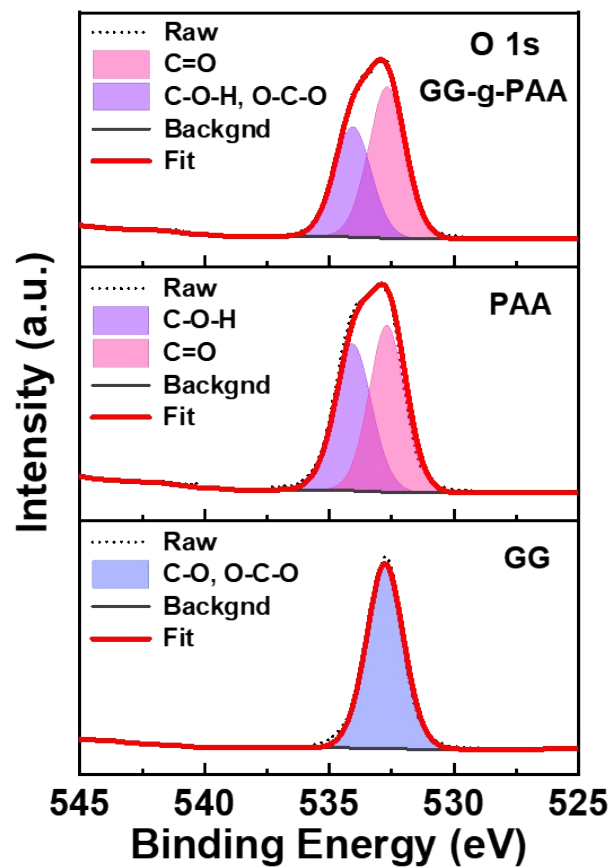


**Fig. S4** Synthesis scheme of the GG-g-PAA binder by free radical ring-opening graft polymerization reaction.

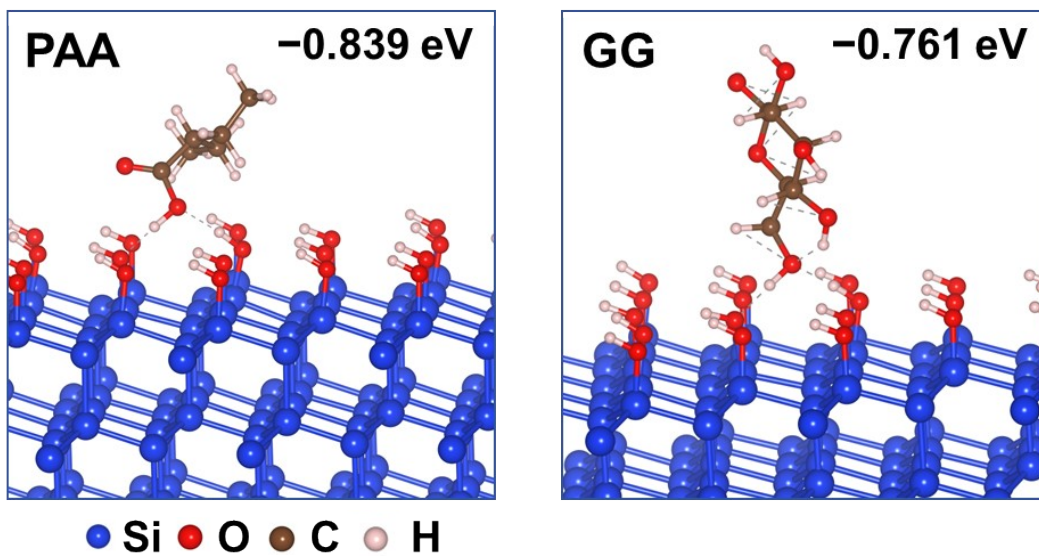


**Fig. S5** (a–d) X-ray energy spectrum of top-viewed SEM image of SiMPs, and corresponding element mapping images of (b) Si, (c) O and (d) C. (e) FTIR spectra of SiMPs and SiMPs/GG-g-PAA (SiMPs:GG-g-PAA = 4:1 w/w).

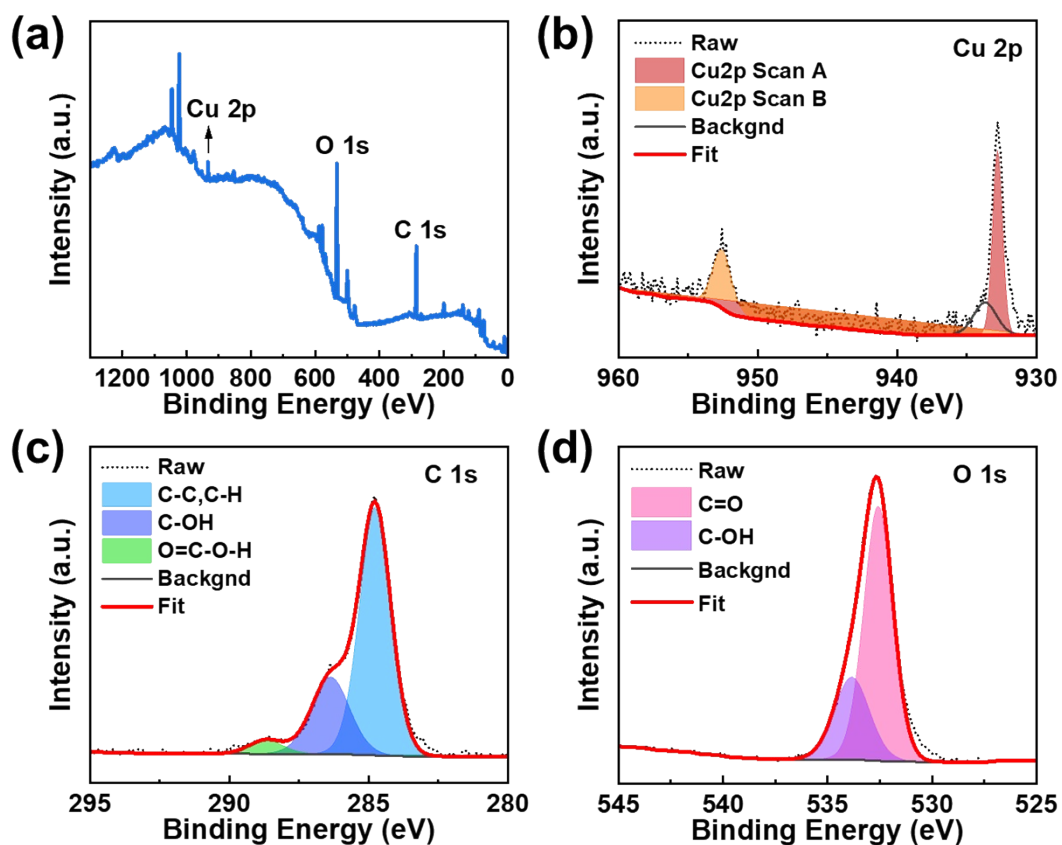
As shown in Fig. S5c and S5e, the abundance of O element on the surface of SiMPs and the obvious O–H characteristic peak in the FTIR spectrum of SiMPs indicate the presence of a large number of silanol groups (Si–OH) on the surface of SiMPs. Compared with SiMPs, the O–H peak shifts to a lower wavenumber at 3410 cm<sup>-1</sup> after mixing with the GG-g-PAA binder, which is due to the electron density change of hydroxyl groups caused by the formation of hydrogen bonds.<sup>12, 13</sup>



**Fig. S6** O 1s XPS spectra of GG, PAA, and GG-g-PAA.

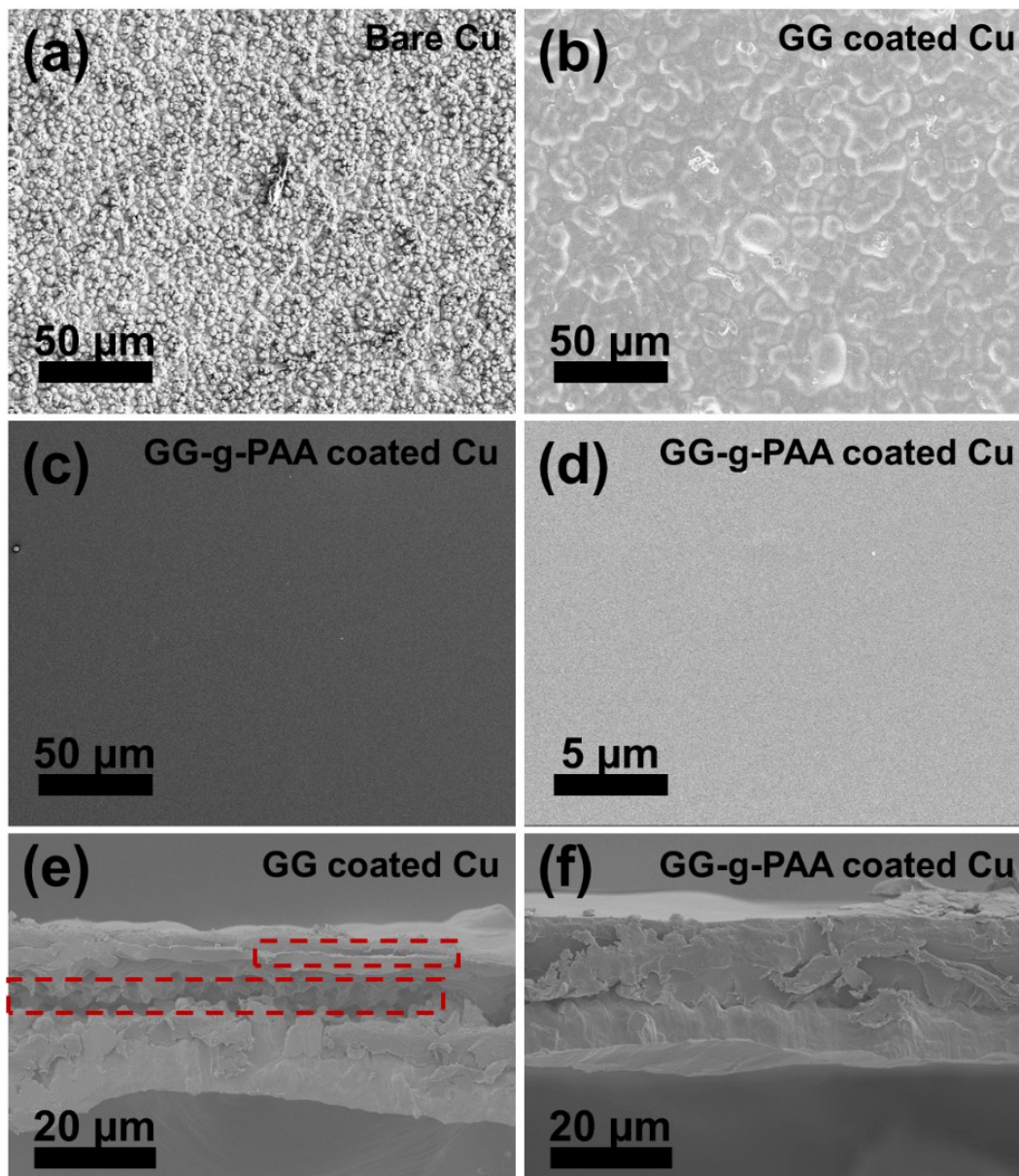


**Fig. S7** The interfacial adhesion energies of the simplified PAA/Si and GG/Si models.



**Fig. S8** (a) XPS spectrum of bare Cu foil. (b) Cu 2p, (c) C 1s, and (d) O 1s XPS spectra of bare copper current collector.

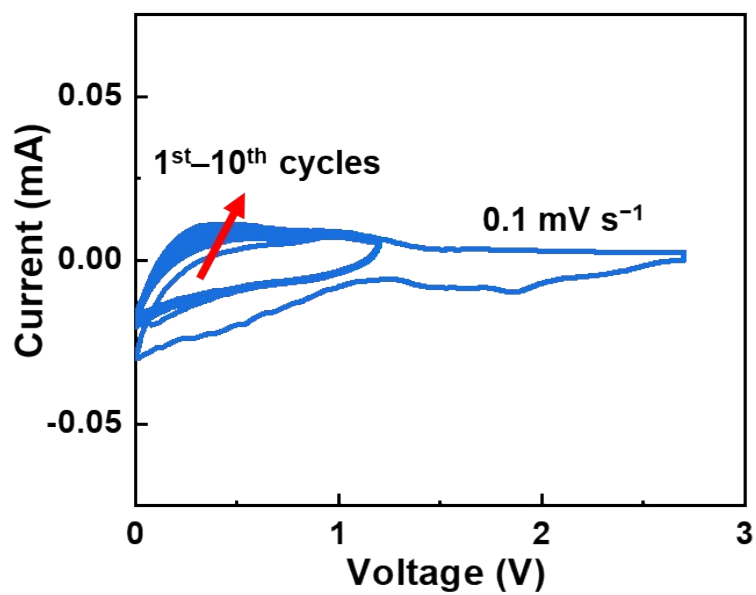
XPS results of bare Cu foil exhibit that its surface is similar to the SiMPs, as both containing a large number of O-containing polar groups.



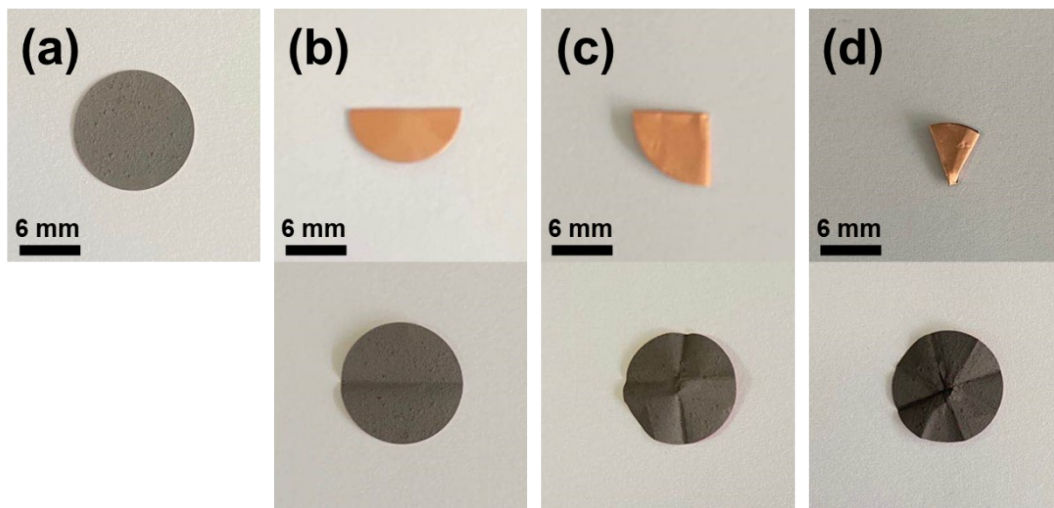
**Fig. S9** (a and b) Top-viewed SEM images of (a) bare Cu foil, (b) GG coated Cu foil. (c and d) Top-viewed SEM images of GG-g-PAA coated Cu foil at varying magnification levels. (e and f) Cross-sectional SEM images of (e) GG coated Cu foil and (f) GG-g-PAA coated foil.

Fig. S9a exhibits Cu foil has a rough surface similar to that of SiMPs. Despite being covered by GG, the surface remains rough, and the bumps on the surface are still clearly visible (Fig. S9b). In contrast, the Cu foil covered by GG-g-PAA appears very smooth and dense even under high-resolution SEM (Fig. S9d), indicating the superior coverage capability of the GG-g-PAA binder. The cross-sectional morphology of the different

binder coated Cu foils is consistent well with their top-viewed morphology. As shown in Fig. S9e, the cross-sectional SEM image of the GG-coated Cu foil reveals significant separation between the Cu foil and the GG film, further suggesting that GG is inadequate for effective coverage. Moreover, the GG film displays noticeable separation attributable to its poor cohesive strength. Conversely, the GG-g-PAA film conforms closely to the Cu foil without any separation, as illustrated in Fig. S9f. And due to the excellent cohesive strength of GG-g-PAA, the GG-g-PAA film itself does not separate.



**Fig. S10** CV curves of the electrode consisting of the GG-g-PAA binder and SP with a mass ratio of 1:1 at a scan rate of  $0.1 \text{ mV s}^{-1}$ .



**Fig. S11** Photographs of a high-loading SiMP@GG-g-PAA electrode during the folding tests. Si loading:  $1.8 \text{ mg cm}^{-2}$ .

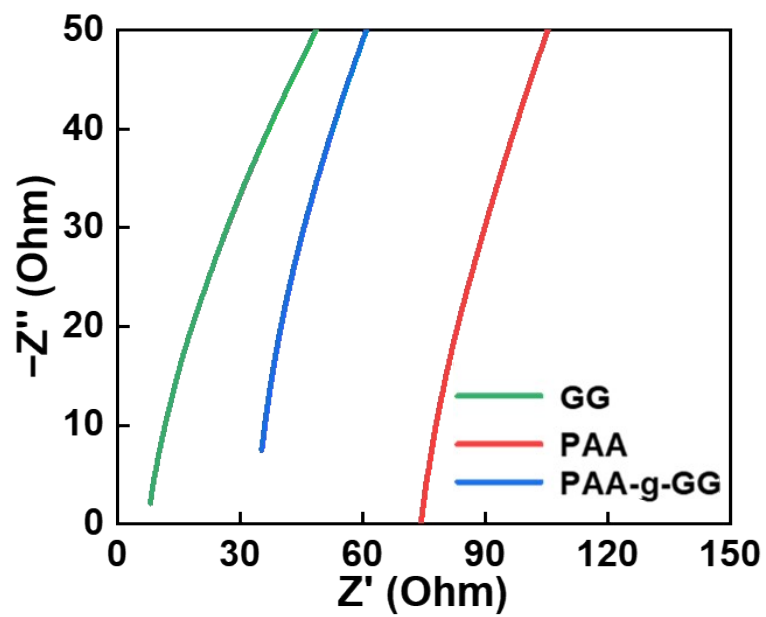


**Fig. S12** EIS results for calculation of ionic conductivity of the different binder films.

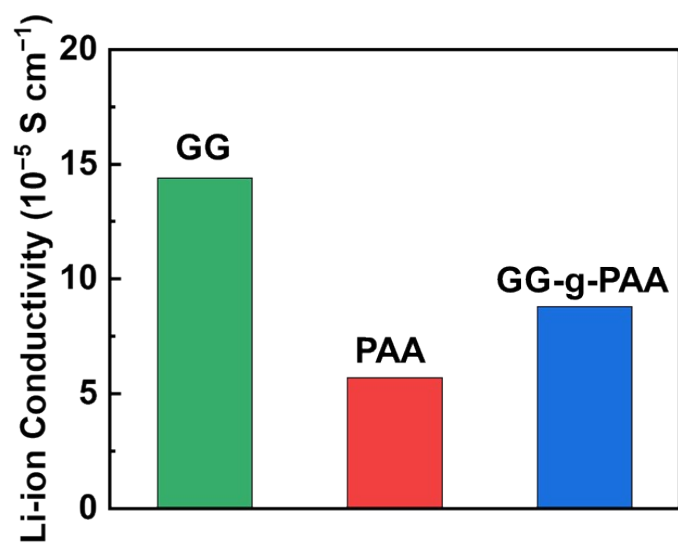


**Fig. S13** Li-ion conductivities of the different binders.

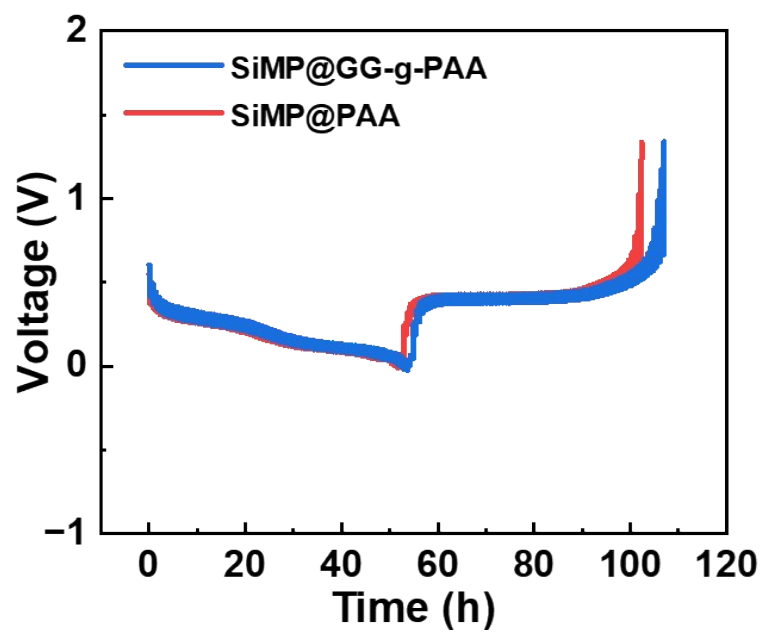


**Fig. S14** GITT curves of the SiMP@PAA and SiMP@GG-g-PAA electrodes.

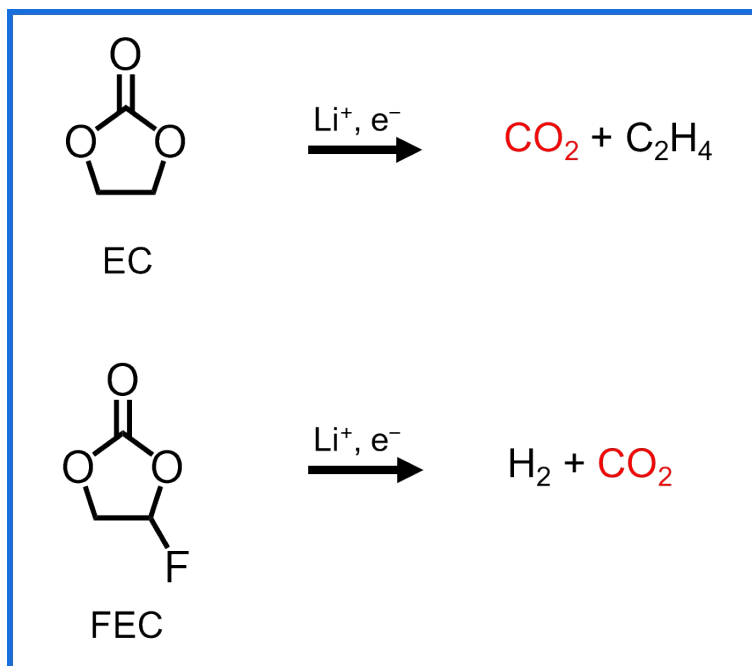


**Fig. S15** The proposed main gas species generated by the reductive decomposition of EC and FEC.

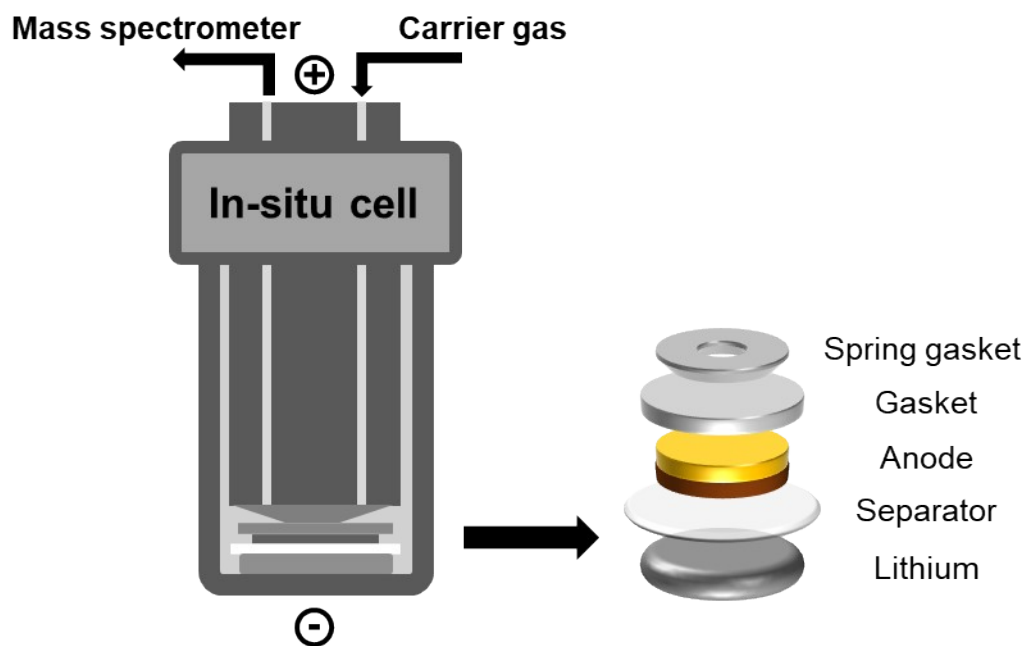


**Fig. S16** Schematic illustration of the in-situ cell setting for in-situ DEMS measurements.

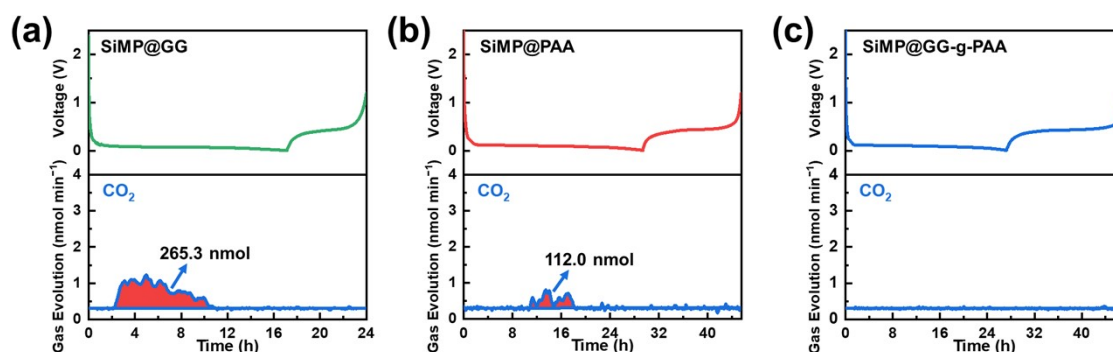


**Fig. S17** (a–c) Detected CO<sub>2</sub> generation of (a) SiMP@GG, (b) SiMP@PAA, and (c) SiMP@GG-g-PAA electrodes during initial charging-discharging cycle.

During in-situ DEMS the measurements, Ar with a flow rate of 3.6 mL min<sup>-1</sup> was vented into the in-situ cell while the mass spectrometer continuously detected the composition of the gas. As shown in Fig. S17a and S17b, the detected CO<sub>2</sub> signal in the middle of initial discharge process of SiMP@GG and SiMP@PAA is particularly obvious. By integrating the detected CO<sub>2</sub> release rate, it is found that the total detected CO<sub>2</sub> generation for SiMP@GG and SiMP@PAA anodes were 265.3 nmol and 112.0 nmol, respectively. This can be due to the fact that the GG and PAA binders are unable to accommodate the huge volume expansion of SiMPs and keep the pulverized SiSMPs coalesced, thereby causing severe destruction of the mechanical structure of the SiMP electrode and rupture of solid electrolyte interphase. Consequently, a large amount of EC and FEC is decomposed to repair the ruptured SEI. In contrast, the GG-g-PAA binder enables to accommodate the huge volume changes of SiMPs and maintain the firm coalescence of pulverized SiMPs without disintegration, resulting in a stable electrode-electrolyte interface and mechanical structure of SiMP anodes during cycling, thus no significant CO<sub>2</sub> was detected (Fig. S17c). Notably, limited by the sensitivity of the measurements, no significant CO<sub>2</sub> signal at the stage of the initial decomposition of FEC and EC to form the pristine SEI was observed for all SiMP electrodes. This suggests the actual CO<sub>2</sub> generation during the initial charging-discharging process is much higher than the detectable level. Nevertheless, the significant difference in detectable CO<sub>2</sub> generation under same measurement condition of different SiMP electrodes confirms the superior role of the GG-g-PAA binder in stabilizing the

electrode-electrolyte interface. Furthermore, although the initial Coulombic efficiency (ICE) of the SiMP@GG-g-PAA electrode achieved in the DEMS measurement is much higher than that of the SiMP@GG and SiMP@PAA electrodes, the disparity between the in-situ DEMS cell configuration and the conventional coin cell configuration for electrochemical performance measurement results in the ICE of the SiMP@GG-g-PAA electrode in the in-situ DEMS cell being markedly lower than that of the SiMP@GG-g-PAA electrode in the conventional coin cell.

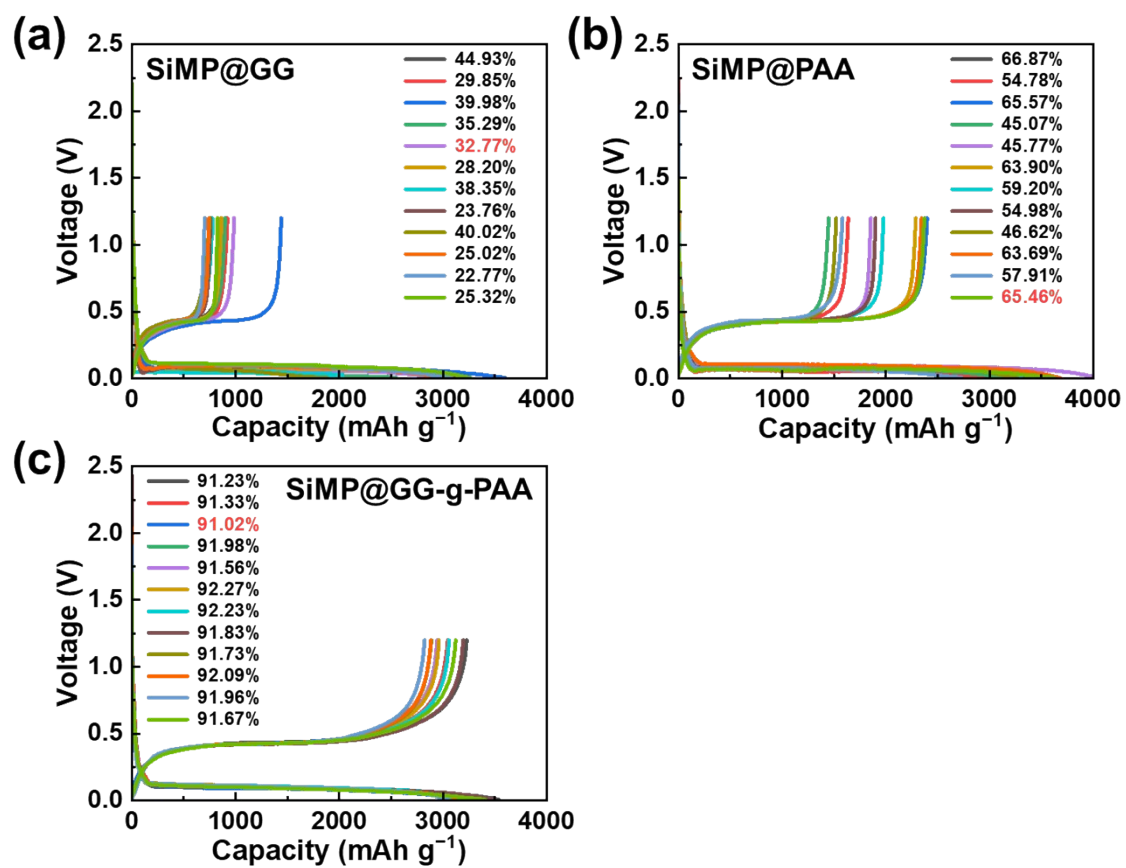


**Fig. S18** (a–c) Initial charge-discharge curves of twelve individual (a) SiMP@GG, (b) SiMP@PAA, and (c) SiMP@GG-g-PAA electrodes when measured at 0.03 C.

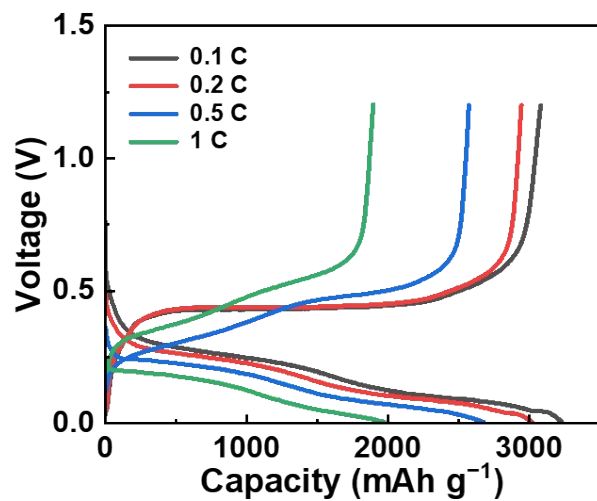


**Fig. S19** Charge-discharge curves of the SiMP@GG-g-PAA electrode at various current rates.

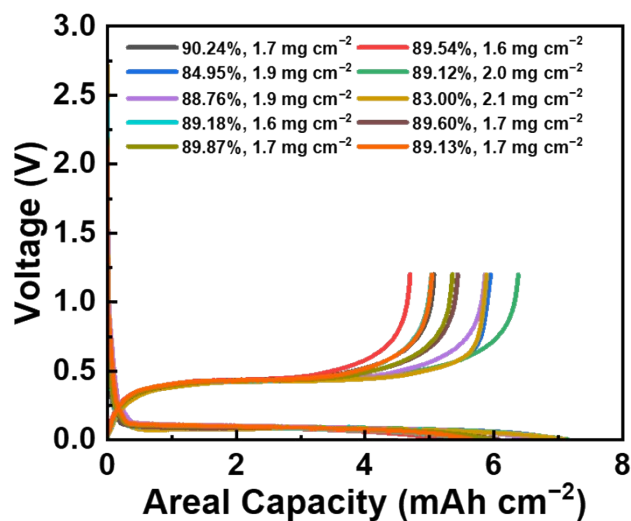


**Fig. S20** Initial charge-discharge curves of ten individual high-loading SiMP@GG-g-PAA electrode when measured at 0.03 C. Si loadings: 1.6–2.1  $\text{mg cm}^{-2}$ .

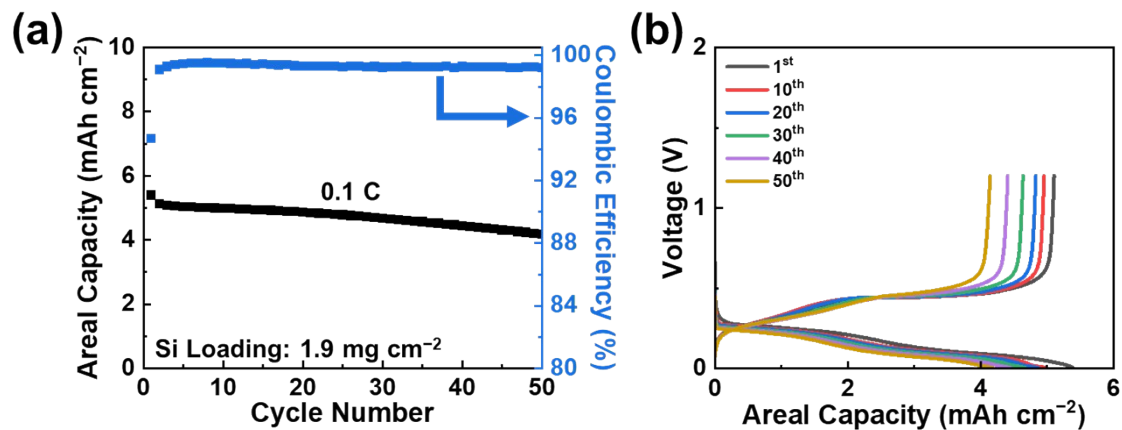


**Fig. S21** (a) Cycling performance of the high-loading SiMP@GG-g-PAA electrode at 0.1 C. (b) Charge-discharge curves of the high-loading SiMP@GG-g-PAA electrode of various cycles at 0.1 C. Si loading:  $1.9 \text{ mg cm}^{-2}$ .

The high-loading SiMP@GG-g-PAA electrode (Si loading:  $1.9 \text{ mg cm}^{-2}$ ) maintains a high areal capacity of  $4.2 \text{ mAh cm}^{-2}$  after 50 cycles at 0.1 C, corresponding to a capacity retention of 77.4%.

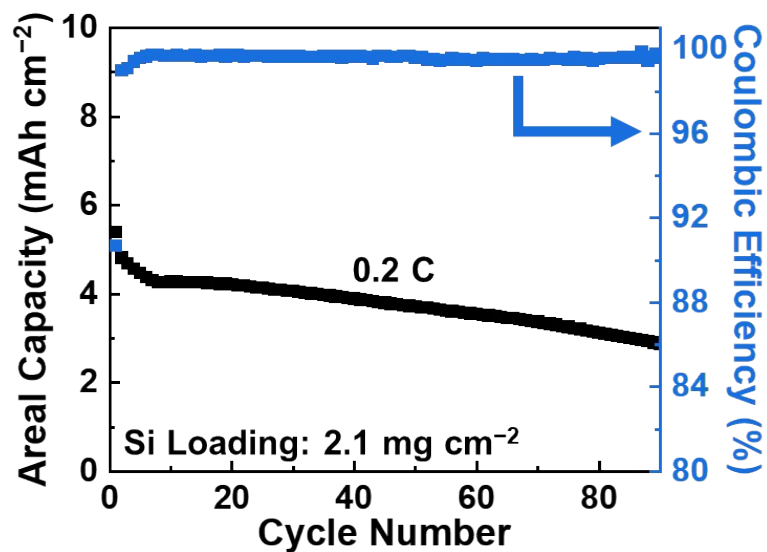


**Fig. S22** Cycling performance of the high-loading SiMP@GG-g-PAA electrode at 0.2 C. Si loading: 2.1 mg cm<sup>-2</sup>.

When cycled at 0.2 C, the SiMP@GG-g-PAA electrode with a high Si loading of 2.1 mg cm<sup>-2</sup> is cycled over 3.0 mAh cm<sup>-2</sup> for about 90 cycles with an average CE of 99.5%.

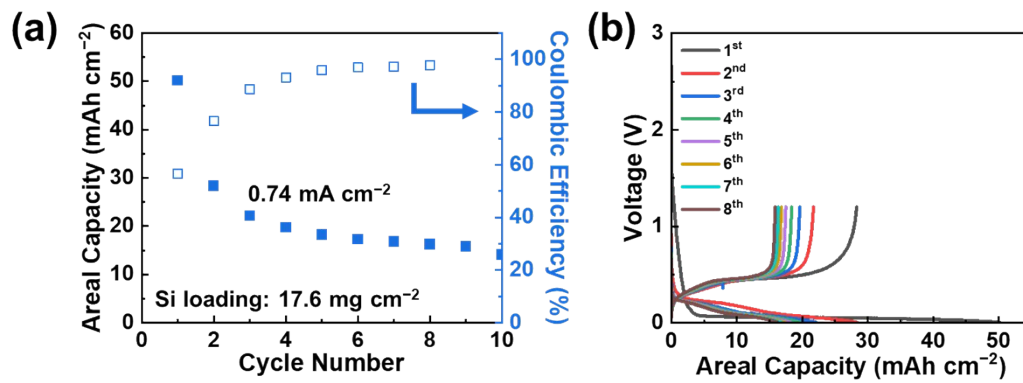


**Fig. S23** (a) Cycling performance and (b) charge-discharge curves of the ultrahigh-loading SiMP@GG-g-PAA electrode at 0.74 mA cm<sup>-2</sup>. Si loadings: 17.6 mg cm<sup>-2</sup>.

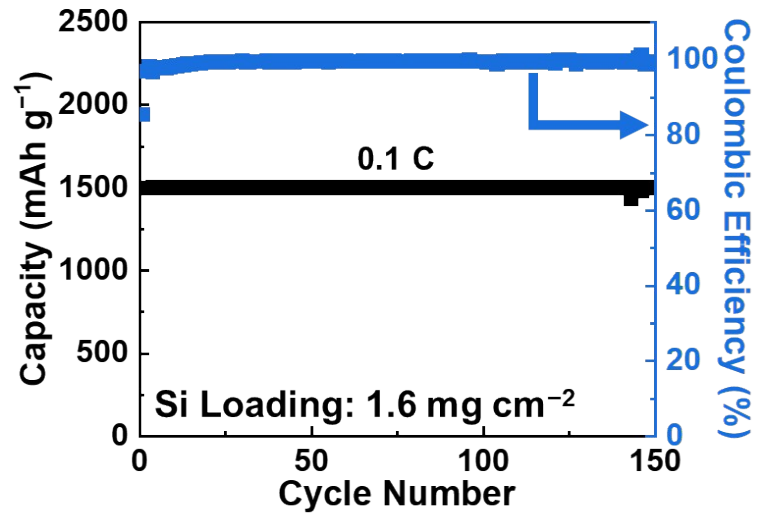


**Fig. S24** Cycling performance of the SiMP@GG-g-PAA electrode with a limited discharge capacity of 1500 mAh g<sup>-1</sup> at 0.1 C. Si loading: 1.6 mg cm<sup>-2</sup>.

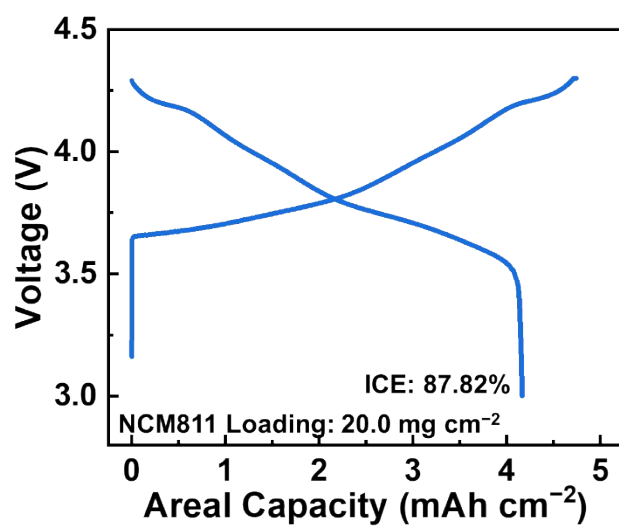


**Fig. S25** Initial charge-discharge curves of the NCM811 cathode at 0.03 C (1 C = 188 mA g<sup>-1</sup>). NCM811 loading: 20.0 mg cm<sup>-2</sup>.

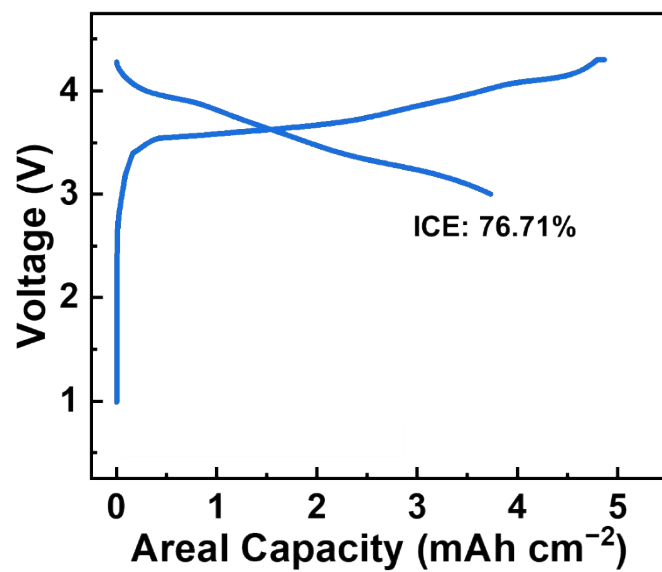


**Fig. S26** Initial charge-discharge curves of the NCM811/SiMP@GG-g-PAA coin-type full cell when measured at 0.03 C. NCM811 loading: 20.1 mg cm<sup>-2</sup>.

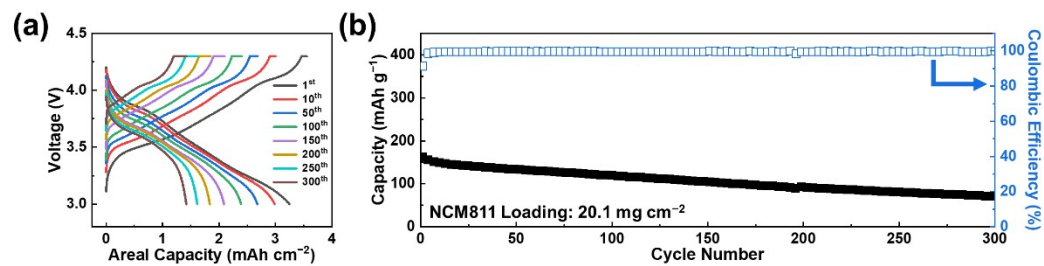


**Fig. S27** (a) Charge-discharge curves and (b) Discharge capacities of the NCM811/SiMP@GG-g-PAA coin-type full cell of various cycles at 0.2 C. NCM811 loading: 20.1 mg cm<sup>-2</sup>.

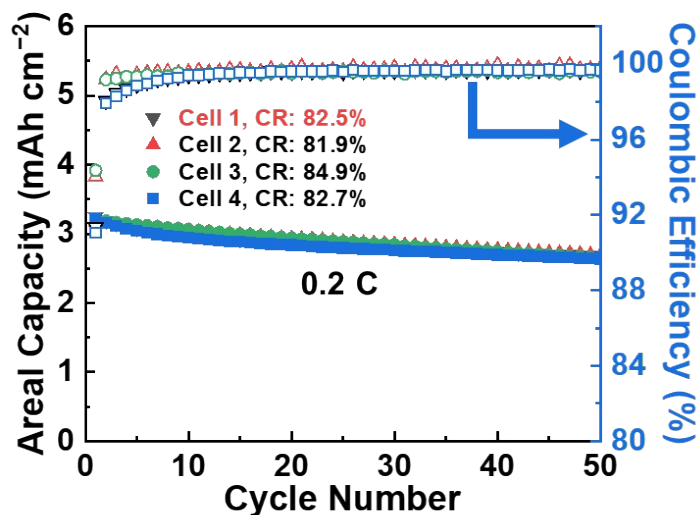


**Fig. S28** Cycling performance of four individual NCM811/SiMP@GG-g-PAA coin-type full cells at 0.2 C. NCM811 loadings: 19.9–20.3 mg cm<sup>-2</sup>.

All four individual high-loading full cells are cycled stably under high areal capacity, all maintaining high areal capacities of over 2.6 mAh cm<sup>-2</sup> and exhibiting high capacity retentions falling within the range of 82 to 85% after 50 cycles at 0.2 C. Such highly consistent and stable cycling performances of these coin-type full cells based on SiMP@GG-g-PAA anode strongly confirm the high reproductivity of the SiMP@GG-g-PAA anodes.

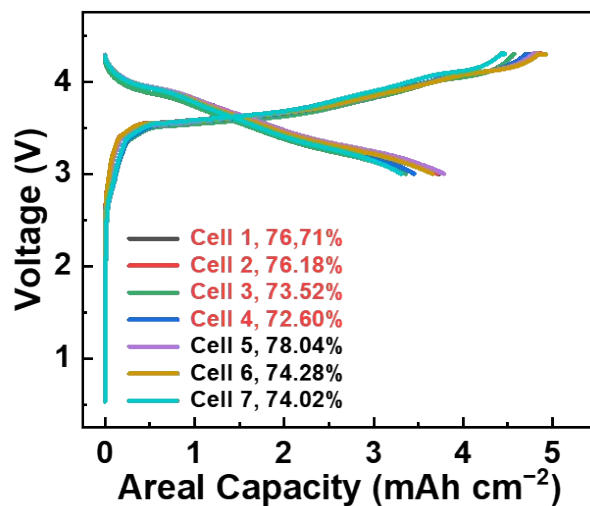


**Fig. S29** Initial charge-discharge curves of seven individual NCM811/SiMP@GG-g-PAA coin-type full cells when measured at 0.03 C. NCM811 loadings: 19.9–20.3 mg cm<sup>-2</sup>.

Seven individual high-loading full cells including four cells in Fig. S28 exhibit ICEs falling within the range of 73 to 78% with an average ICE of 75.05%. Such relatively high and comparable ICEs of full cells further reconfirm the high reproducibility of the SiMP@GG-g-PAA electrodes.

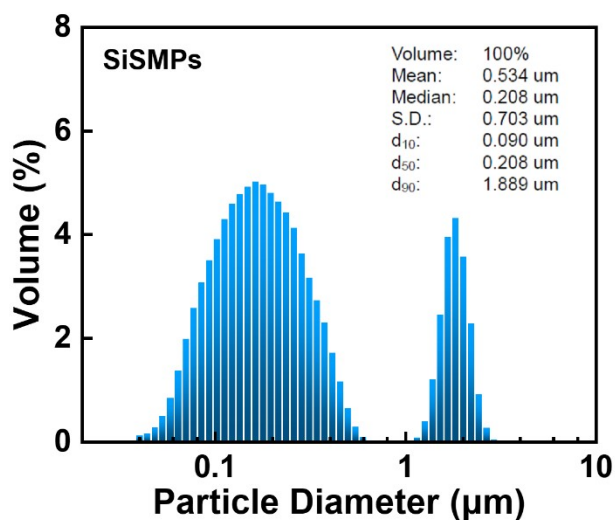


**Fig. S30** Size distribution of SiSMPs.

As shown in Fig. S30, after ball milling for 20 h, the average particle size of SiSMPs (0.53 µm) is significantly smaller than that of SiMPs (0.98 µm). Additionally, the volume of particles smaller than 150 nm increases significantly. Despite these changes, the majority of particles remained larger than 150 nm, implying that while the issue of particle pulverization in the SiSMP electrodes has been mitigated compared to SiMPs, it still persists to a significant extent.

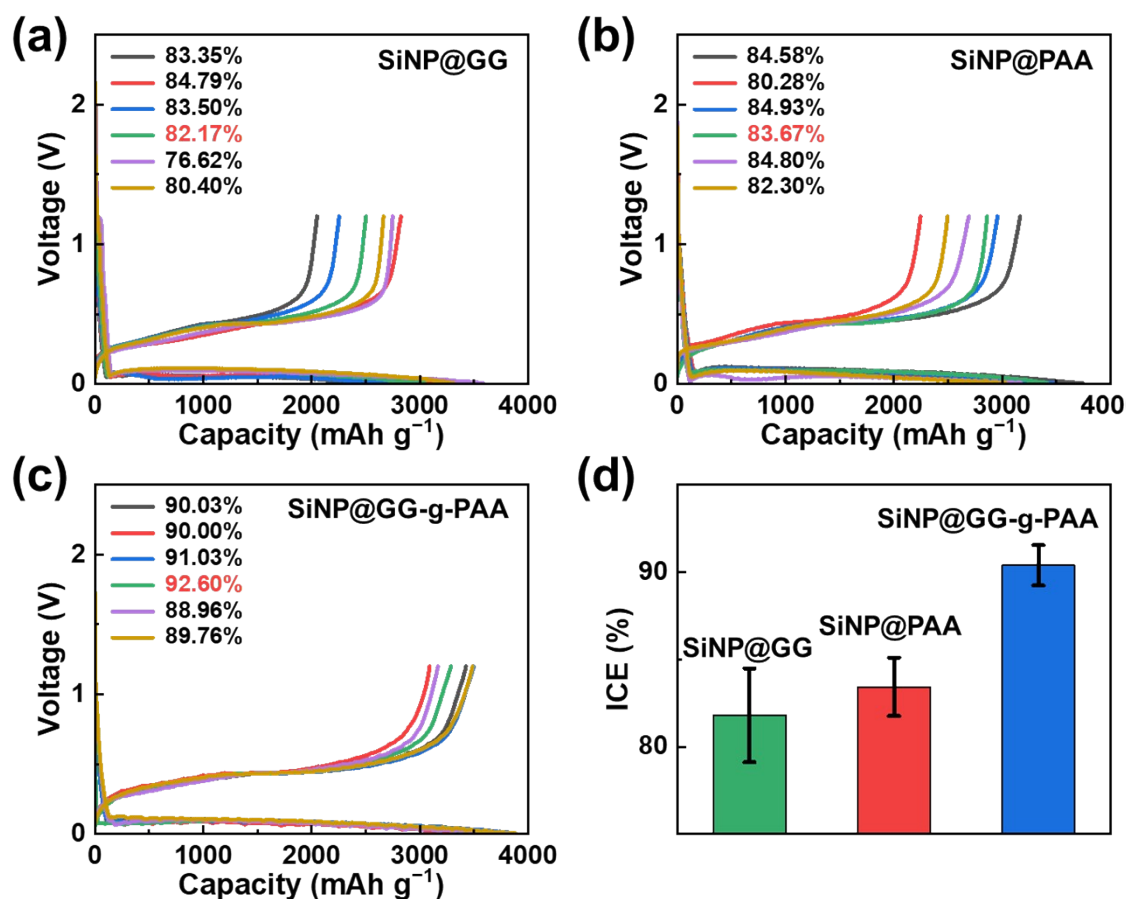


**Fig. S31** (a–c) Initial charge-discharge curves of six individual (a) SiNP@GG, (b) SiNP@PAA, and (c) SiNP@GG-g-PAA electrodes when measured at 0.03 C. (d) The average ICEs of the different SiNP anodes. Error bars are the standard deviation of measurement of six individual electrodes. Si loadings: 0.7–1.2 mg cm<sup>-2</sup>.

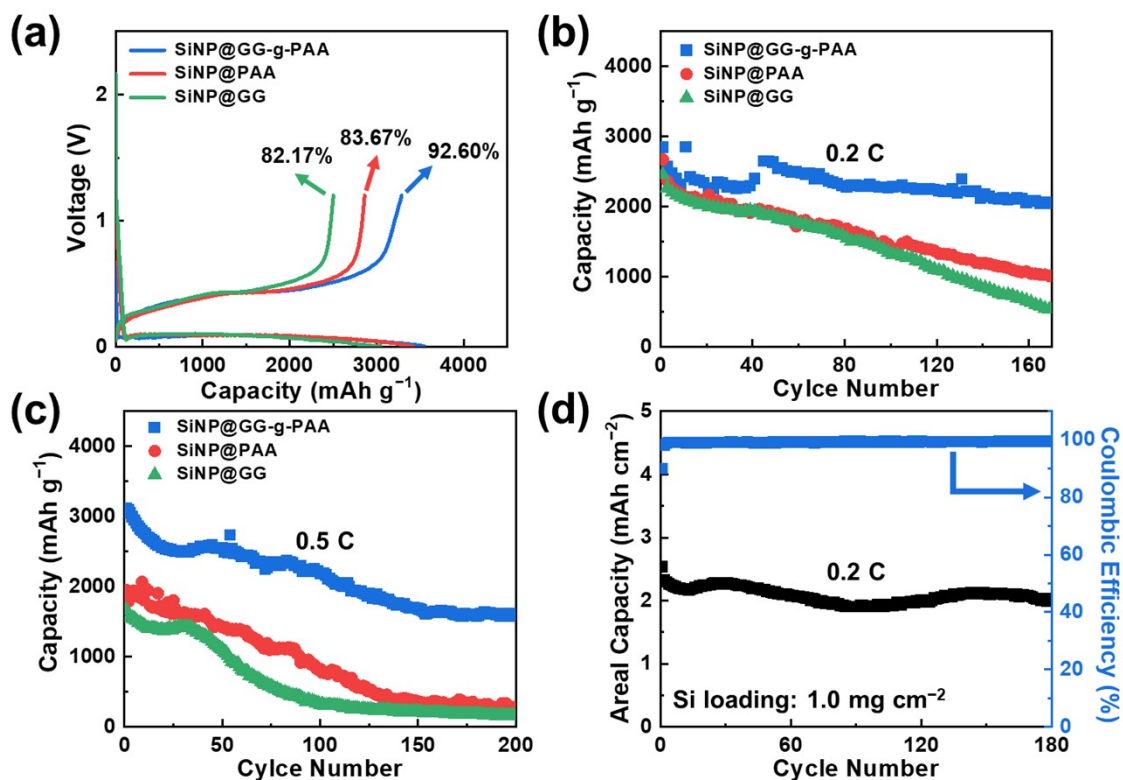


**Fig. S32** (a) Initial charge-discharge curves of different SiNP electrodes when measured at 0.03 C. (b and C) Cycling performance of different SiNP electrodes at (b) 0.2 C and (c) 0.5 C. (d) Cycling performance of the SiNP@GG-g-PAA electrode (SiNPs: SP: binder = 75:10:15 w/w/w) with electrolyte containing 10 vol% FEC. Si loadings: 0.8–1.0 mg cm<sup>-2</sup>.

When cycled at 0.2 C, the SiNP@GG-g-PAA electrode exhibits a high discharge capacity of 2048 mAh g<sup>-1</sup> after 170 cycles, which is 1513 and 1036 mAh g<sup>-1</sup> higher than that of SiNP@GG and SiNP@PAA electrodes, respectively (Fig. S32b). When the current rate increases to 0.5 C, the SiNP@GG-g-PAA still maintains a high discharge capacity of 1594 mAh g<sup>-1</sup> after 200 cycles. In sharp contrast, the same cycles, the SiNP@GG and SiNP@PAA electrodes only maintain the discharge capacities of 156 and 250 mAh g<sup>-1</sup>, respectively (Fig. S32c).

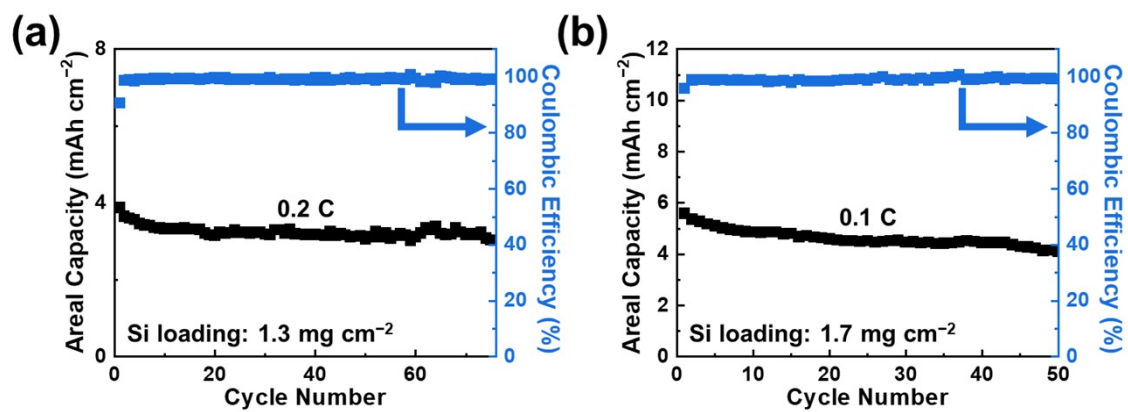


**Fig. S33** (a and b) Cycling performance of high-loading SiNP@GG-g-PAA electrodes at (a) 0.2 C and (b) 0.1 C. Si loadings: (a) 1.3 mg cm<sup>-2</sup> and (b) 1.7 mg cm<sup>-2</sup>.

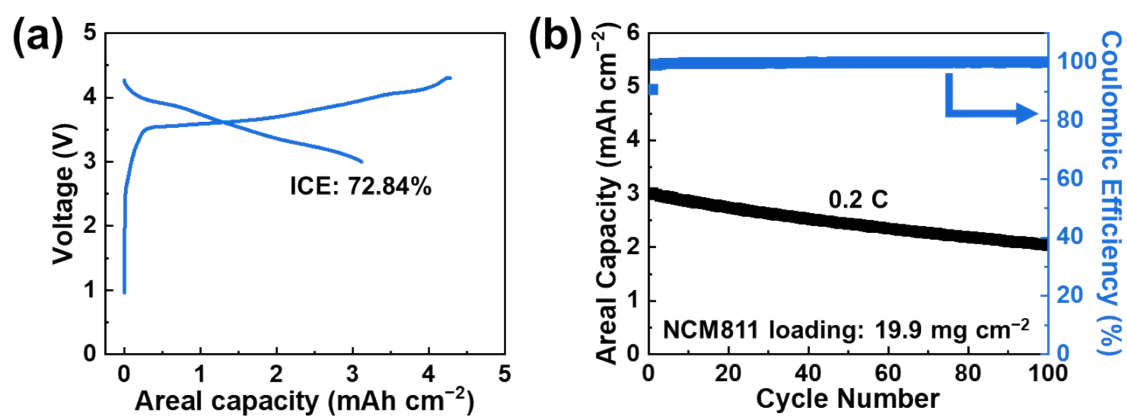


**Fig. S34** (a) Initial charge-discharge curves of the NCM811/SiNP@GG-g-PAA coin-type full cell when measured at 0.03 C. (b) Cycling performance of the NCM811/SiNP@GG-g-PAA coin-type full cell at 0.2 C. NCM811 loading: 19.9 mg cm<sup>-2</sup>.

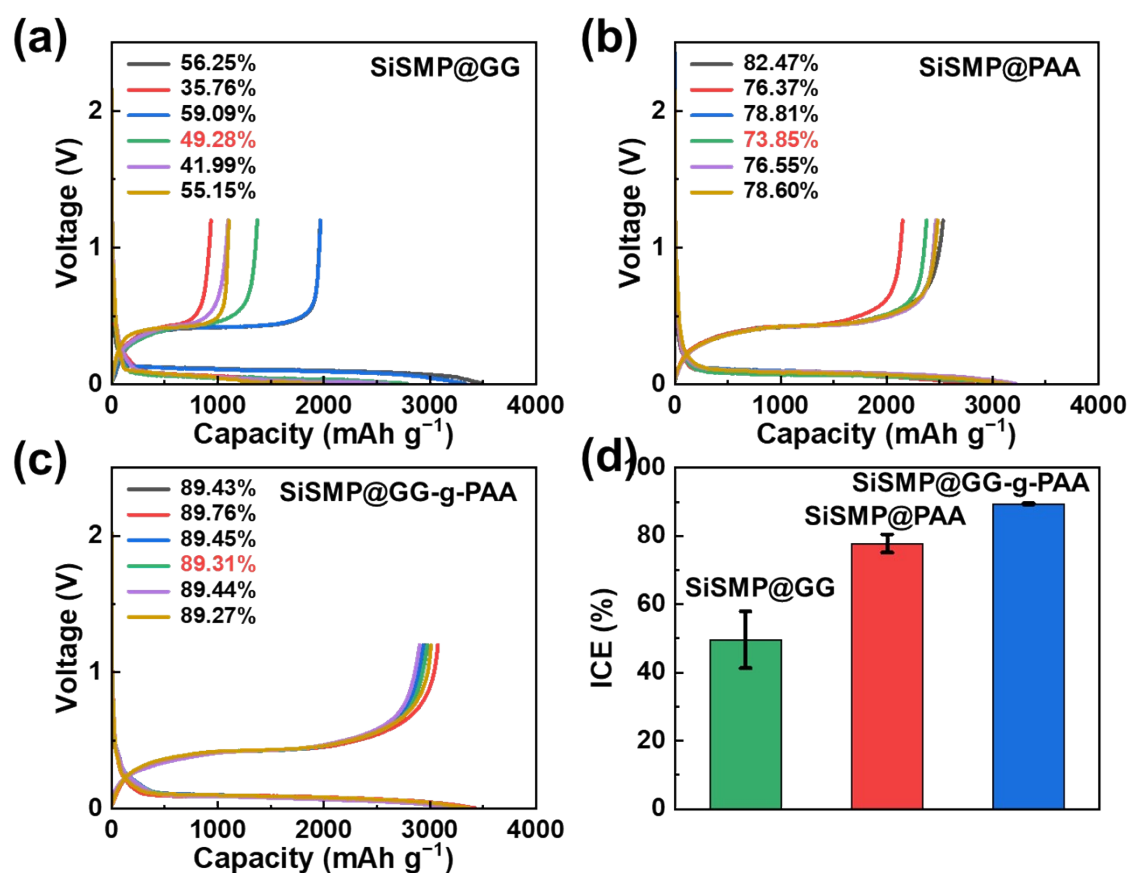


**Fig. S35** (a–c) Initial charge-discharge curves of six individual (a) SiSMP@GG, (b) SiSMP@PAA, and (c) SiSMP@GG-g-PAA electrodes when measured at 0.03 C. (d) The average ICEs of the different SiSMP anodes. Error bars are the standard deviation of measurement of six individual electrodes. Si loadings: 0.8–1.2 mg cm<sup>-2</sup>.

The SiSMP@GG electrode exhibits a low average ICE of 49.59%, suggesting that its mechanical structure is highly damaged during the initial activation cycles, resulting in significantly low irreversible capacity.

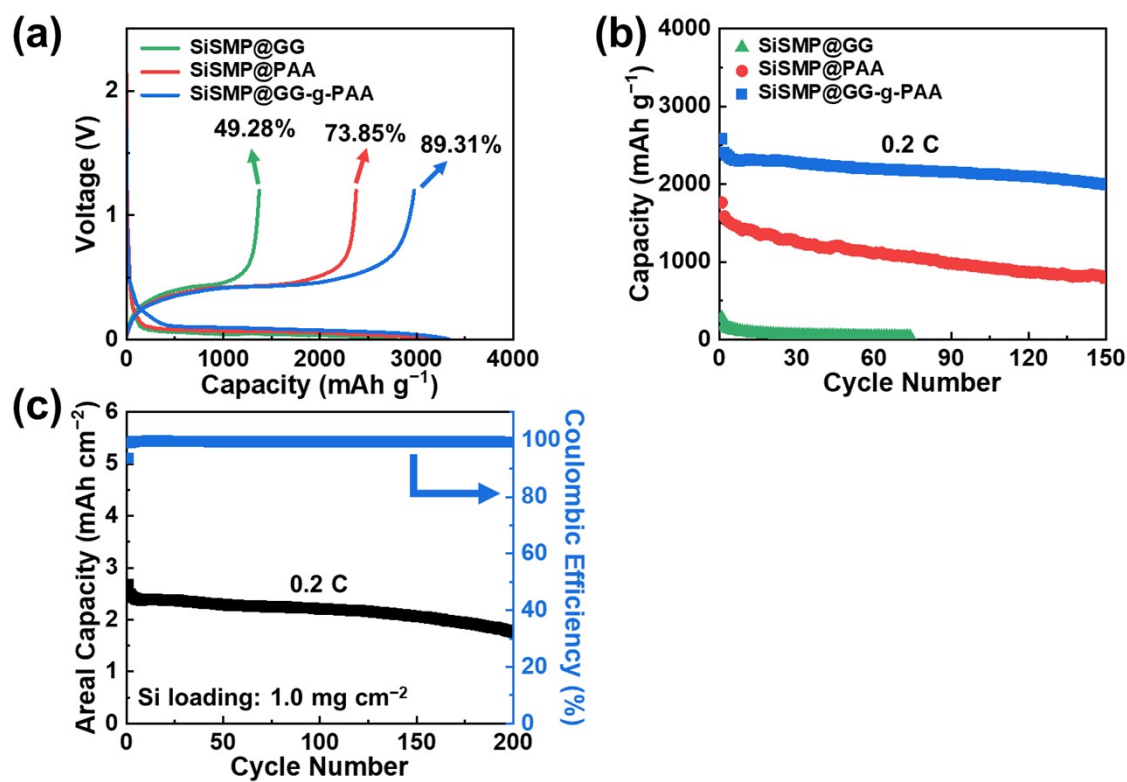


**Fig. S36** (a) Initial charge-discharge curves of different SiSMP electrodes when measured at 0.03 C. (b) Cycling performance of different SiSMP electrodes at 0.2 C. (c) Extended cycling performance of the SiSMP@GG-g-PAA electrode at 0.2 C. Si loadings:  $1.0\text{--}1.1 \text{ mg cm}^{-2}$ .

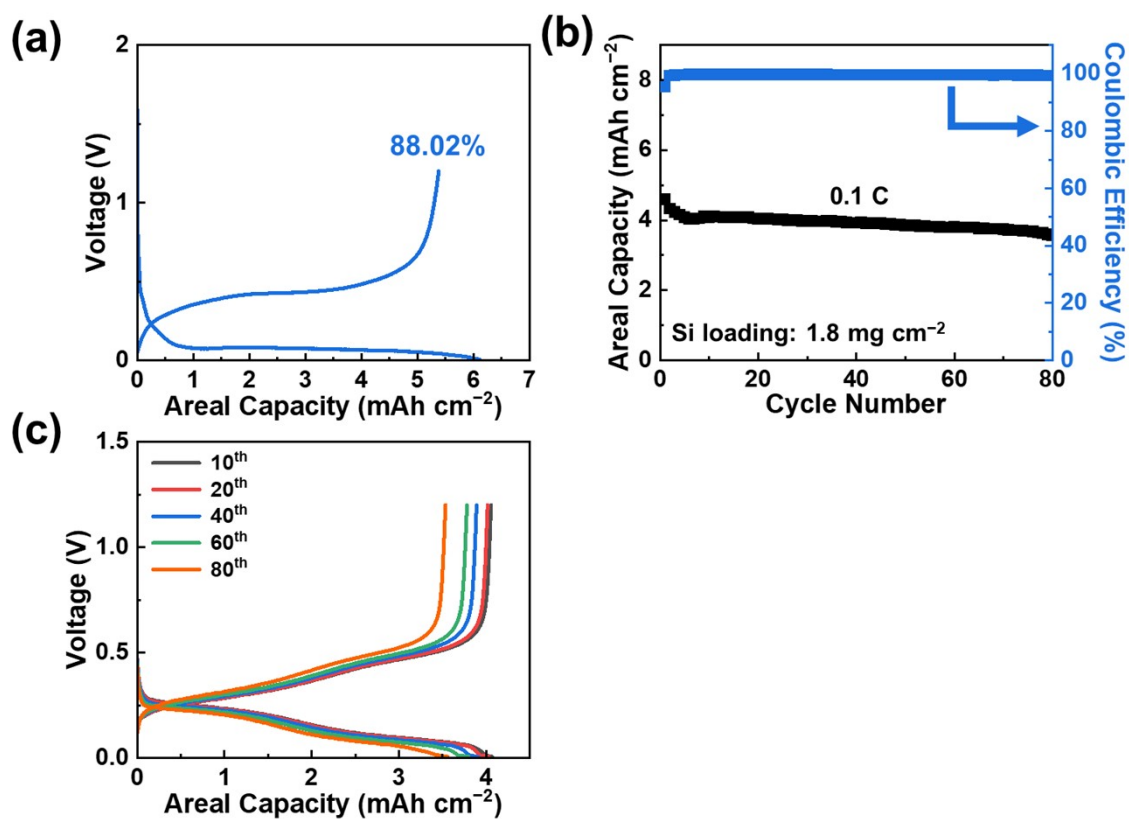


**Fig. S37** (a) Initial charge-discharge curves of the high-loading SiSMP@GG-g-PAA electrode when measured at 0.03 C. (b) Cycling performance and (c) charge-discharge curves of the high-loading SiSMP@GG-g-PAA electrode at 0.1 C. Si loading:  $1.8 \text{ mg cm}^{-2}$ .

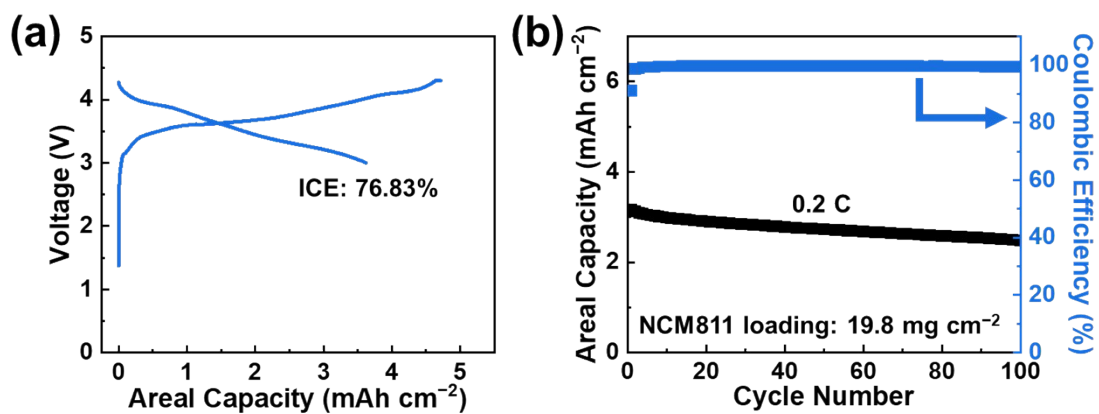


**Fig. S38** (a) Initial charge-discharge curves of the NCM811/SiSMP@GG-g-PAA coin-type full cell when measured at 0.03 C. (b) Cycling performance of the NCM811/SiSMP@GG-g-PAA coin-type full cell at 0.2 C. NCM811 loading: 19.8 mg cm<sup>-2</sup>.

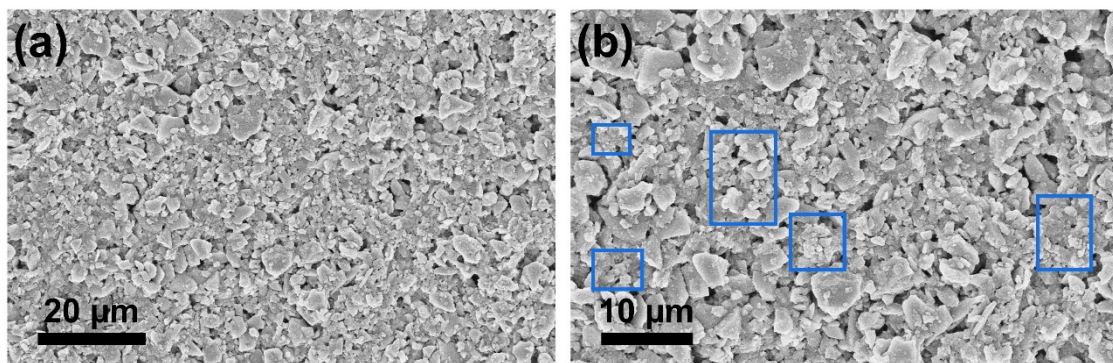


**Fig. S39** (a and b) Top-viewed SEM images of the SiMP@GG-g-PAA electrode at varying magnification levels after 50 cycles at 0.2 C.

The high-resolution SEM images clearly shows that the SiMP@GG-g-PAA maintains the coalescence of pulverized SiMPs and tight connection between SiMPs (Fig. S39b).

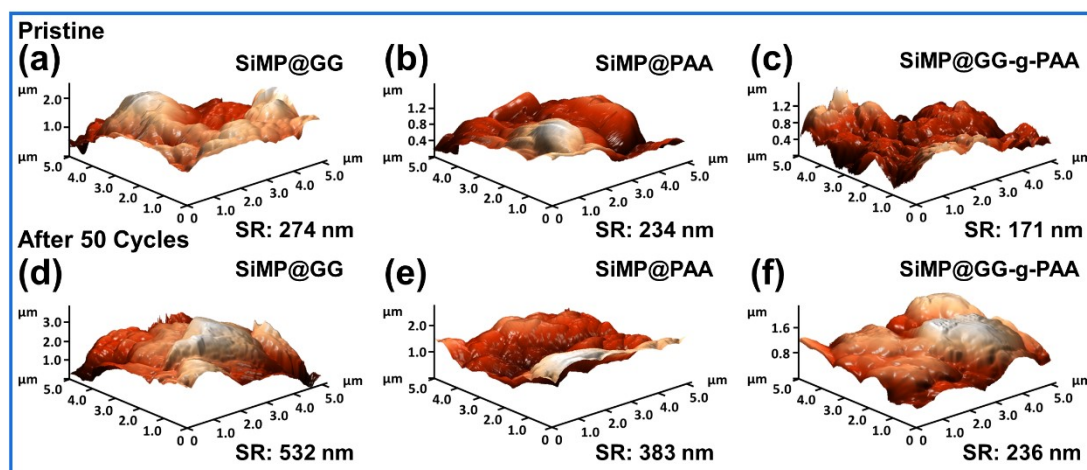


**Fig. S40** (a–c) AFM images of the pristine (a) SiMP@GG, (b) SiMP@PAA, and (c) SiMP@GG-g-PAA electrodes. (d–f) AFM images of the (d) SiMP@GG, (e) SiMP@PAA, and (f) SiMP@GG-g-PAA electrodes after 50 cycles at 0.2 C.

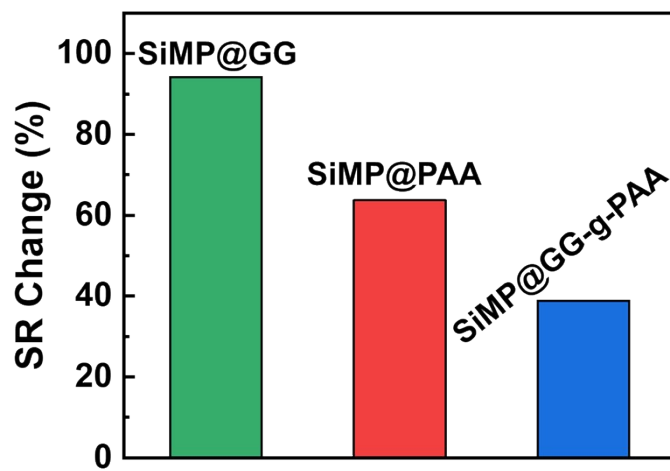


**Fig. S41** Surface roughness changes of the different SiMP electrodes after 50 cycles at 0.2 C.

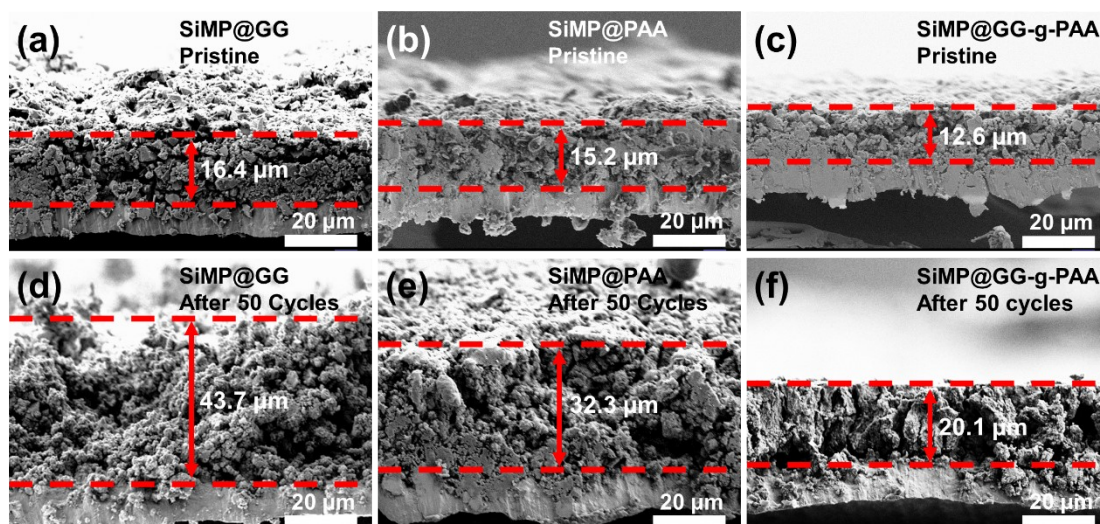


**Fig. S42** (a–c) Cross-sectional SEM images of the pristine (a) SiMP@GG, (b) SiMP@PAA, and (c) SiMP@GG-g-PAA electrodes. (d–f) Cross-sectional SEM images of the (d) SiMP@GG, (e) SiMP@PAA, and (f) SiMP@GG-g-PAA electrodes after 50 cycles at 0.2 C.

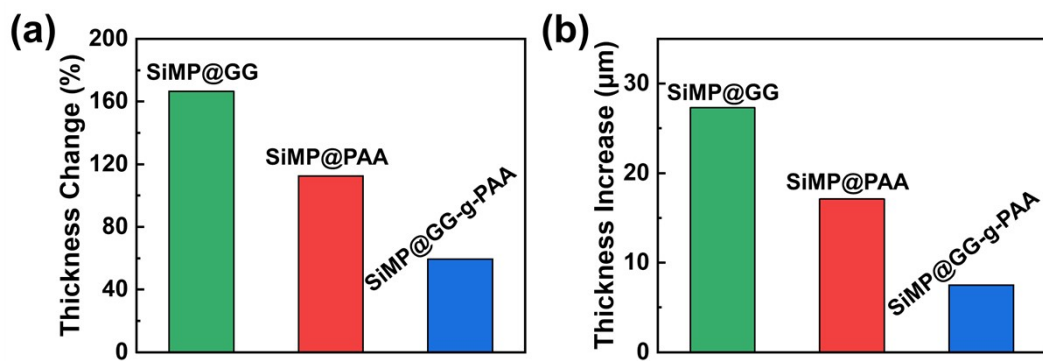


**Fig. S43** Thickness changes of the different SiMP electrodes after 50 cycles at 0.2 C.

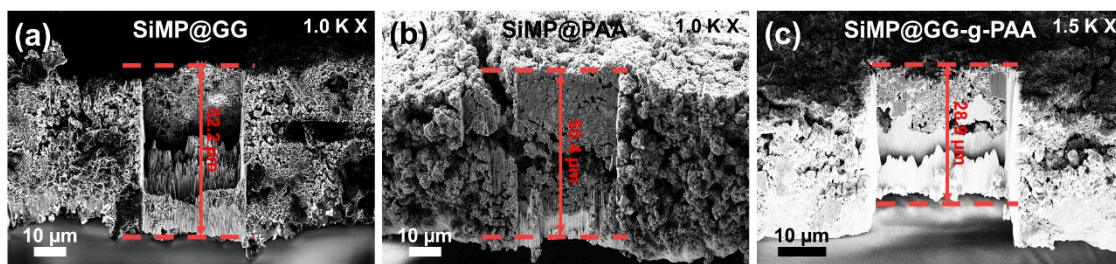


**Fig. S44** (a–c) Cross-sectional FIB-SEM images of the (a) SiMP@GG, (b) SiMP@PAA, and (c) SiMP@GG-g-PAA electrodes after 50 cycles at 0.2 C.

After FIB etching, several SiMPs were deposited on the copper current collector ( $\sim 10 \mu\text{m}$ ), causing a blurred interface between the collector and the electrode film. Therefore, the overall thickness of the collector and the electrode sheet is marked in Fig. S44.



**Fig. S45** (a–c) High-resolution cross-sectional SEM images after FIB etching of the (a) SiMP@GG, (b) SiMP@PAA, and (c) SiMP@GG-g-PAA electrodes after 50 cycles at 0.2 C.

High-resolution cross-sectional SEM images of cycled SiMP electrodes obtained after FIB etching more clearly exhibits the minimal swelling of the SiMP@GG-g-PAA electrodes, maintains close SiMPs contact, and preserves large voids resulting from the irregular shape and high hardness of the SiMPs (Fig. S45c). While the cycled SiMP@GG and SiMP@PAA electrodes exhibit significant swelling and numerous submicron/nano cracks (Fig. S45a and S45b).

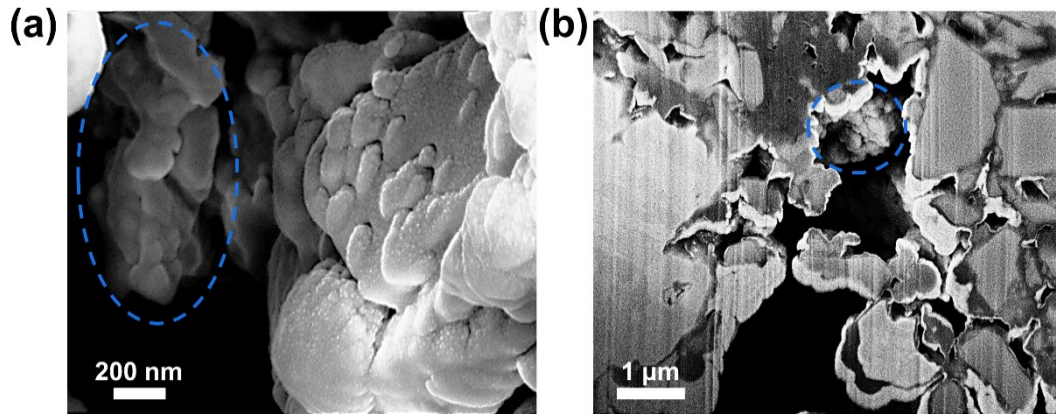


**Fig. S46** (a) The magnified FIB-SEM image of Fig. 7(i). (b) The high-magnification cross-sectional FIB-SEM image of the other area on the cycled SiMP@GG-g-PAA electrode of Fig. 7(h).

Fig. S46 presents higher magnification SEM images of the cycled SiMP@GG-g-PAA electrode from Figure 7i and 7h. Both images exhibit that the pulverized SiMPs remain firmly coalesced, further confirming the superior role of the GG-g-PAA binder in preventing the adherend failure of SiMP anodes.

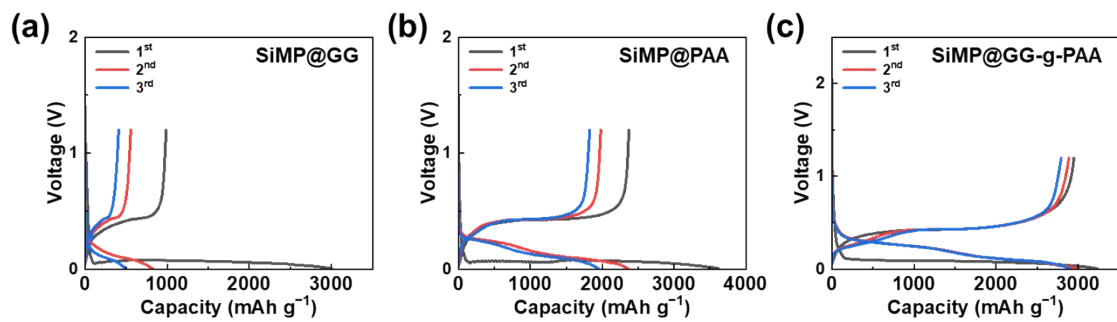


**Fig. S47** (a–c) Charge-discharge curves of the three precycles of (a) SiMP@GG, (b) SiMP@PAA, and (c) SiMP@GG-g-PAA electrodes in Figure 6a and 6b at 0.03 C.

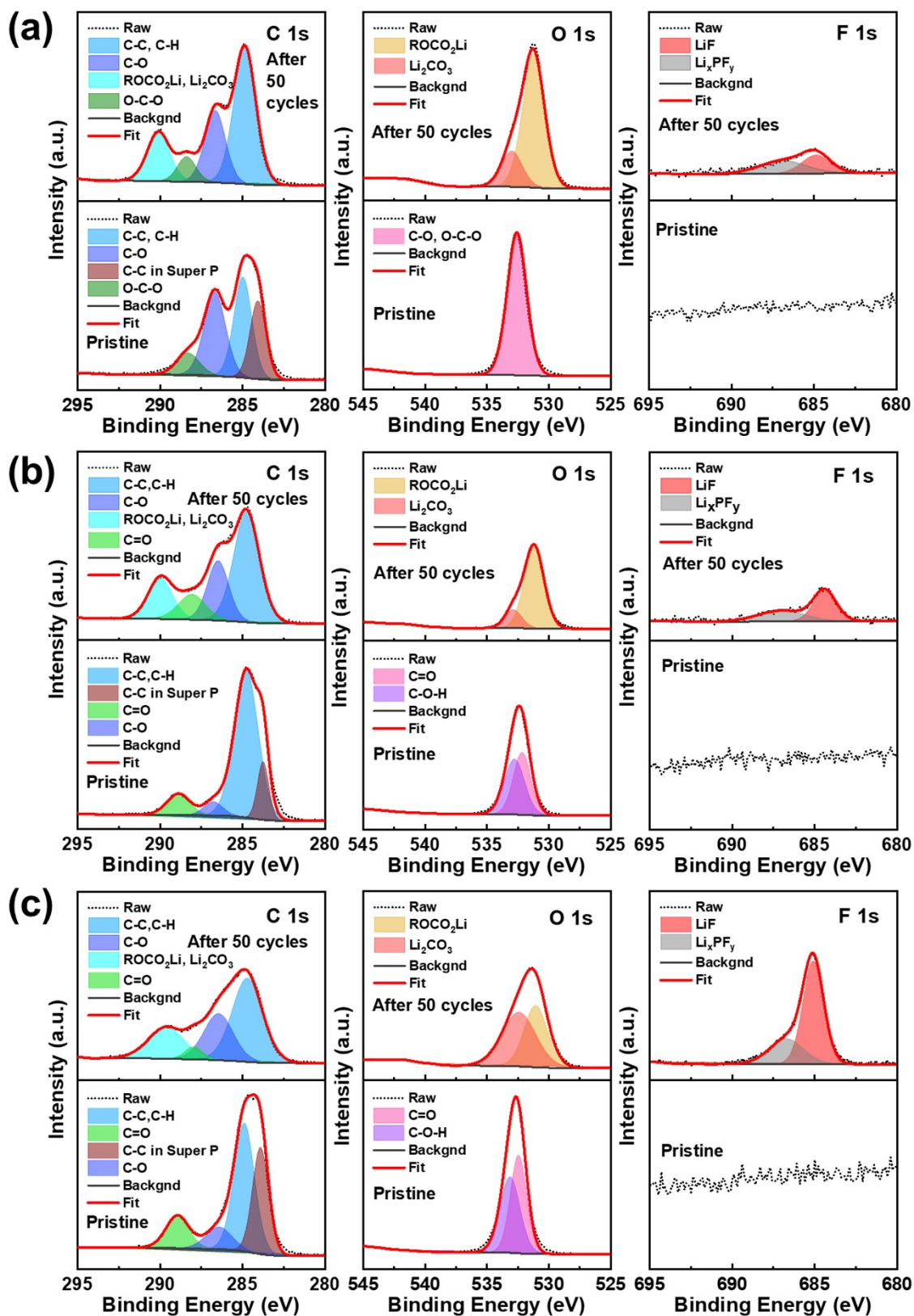


**Fig. S48** (a–c) XPS spectra of pristine and cycled (a) SiMP@GG, (b) SiMP@PAA, (c) SiMP@GG-g-PAA electrodes.

Fig. S48 displays the XPS spectra of the pristine and cycled SiMP electrodes with different binders. After 50 cycles at 0.2 C, the characteristic peaks of  $\text{ROCO}_2\text{Li}$  in the C 1s and O 1s XPS spectra of SiMP@GG-g-PAA exhibits much slower growth than those of SiMP@GG and SiMP@PAA electrodes, accounting for less decomposition of EC and DEC at the SiMP@GG-g-PAA electrode-electrolyte during cycling.<sup>14, 15</sup> The F1s XPS spectrum of the cycled SiMP@GG-g-PAA electrode shows a distinct peak corresponding to LiF, while intensity of the LiF characteristic peak in the F1s XPS spectra of cycled SiMP@GG and SiMP@PAA electrode is both very weak. Besides, the content of LiF in the F1s XPS spectrum of SiMP@GG-g-PAA (71.4%) is also much higher than 57.6% of SiMP@PAA and 46.2% of SiMP@GG electrodes. The XPS results of SiMP electrodes with different binders confirm that the GG-g-PAA binder ensures a stable interfacial chemistry, reduces the excessive decomposition of electrolyte, and hence maintains a dense and thin SEI during deep and continuous cycles.

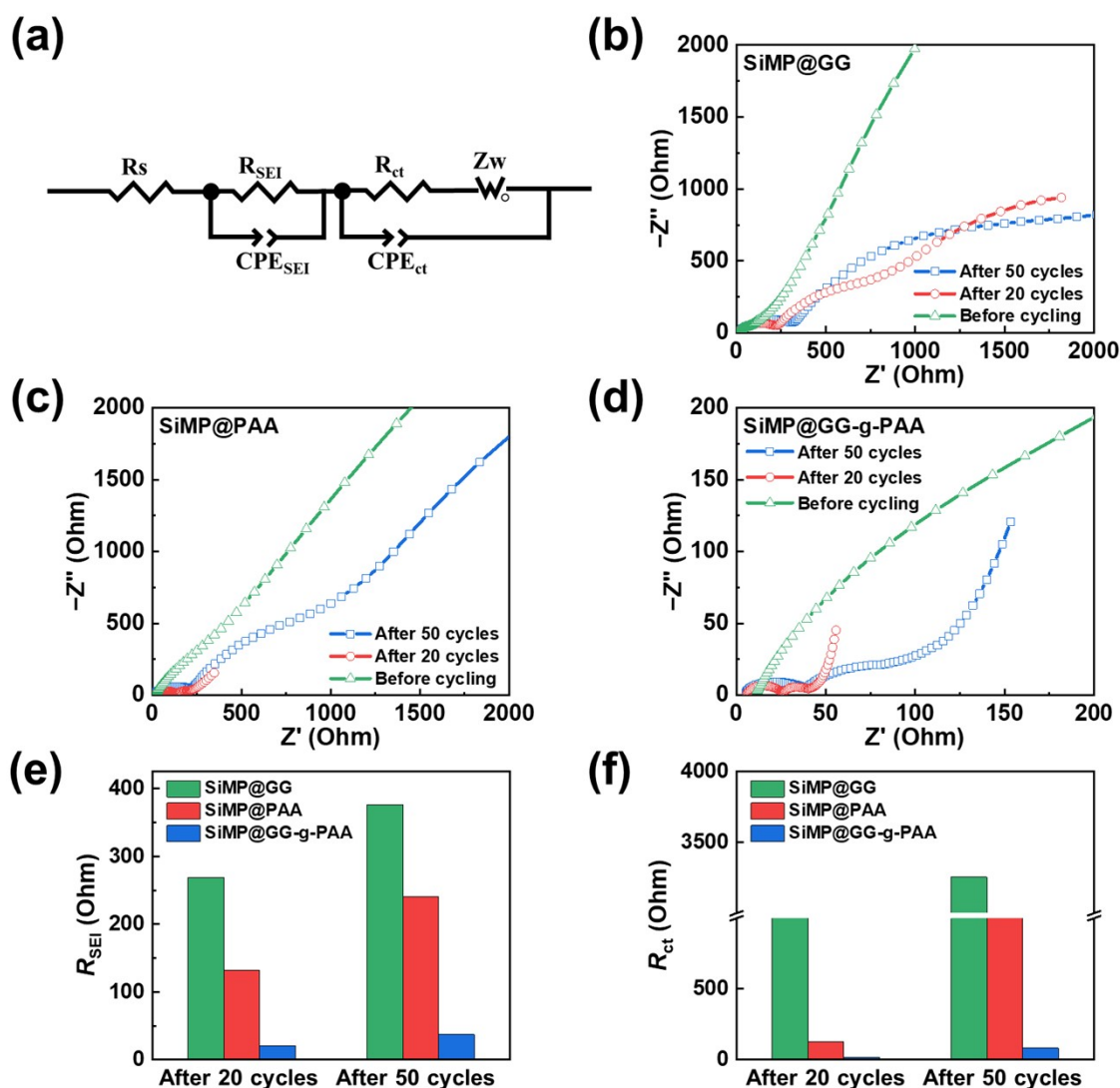


**Fig. S49** (a) The equivalent circuit used for fitting the EIS spectra. (b–d) The EIS spectra of (b) SiMP@GG, (c) SiMP@PAA, and (d) SiMP@GG-g-PAA electrodes before and after cycling. (e)  $R_{SEI}$  of different SiMP electrodes after 20 and 50 cycles at 0.2 C. (f)  $R_{ct}$  of different SiMP electrodes after 20 and 50 cycles at 0.2 C.

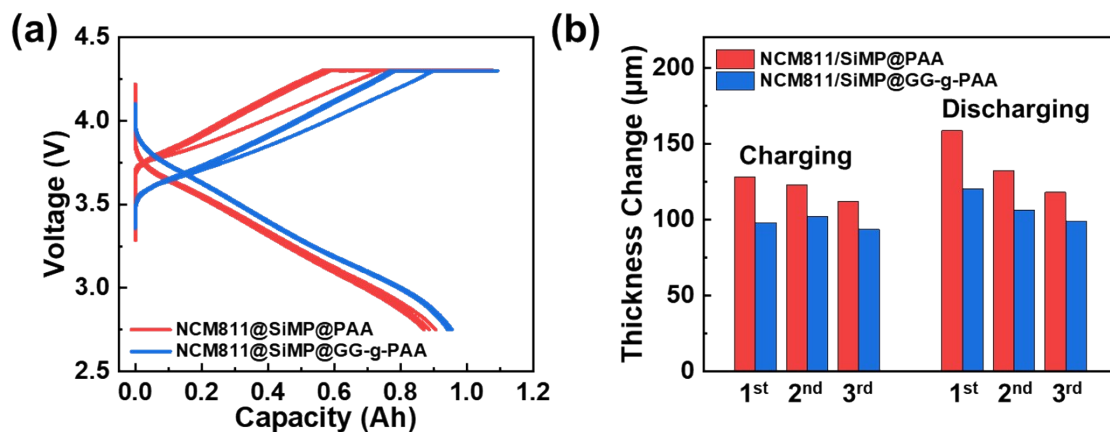


**Fig. S50** (a) Charge-discharge curves of the 6-layer NCM811/SiMP@PAA and NCM811/SiMP@GG-g-PAA pouch cells during the in-situ electrochemical dilatometry measurements at 0.1 C. (b) Thickness changes of 6-layer NCM811/SiMP@PAA and NCM811/SiMP@GG-g-PAA pouch cells after charging and discharging of the first three cycles at 0.1 C.

During the in-situ electrochemical dilatometry measurements, the NCM811/SiMP@GG-g-PAA pouch cell exhibits the higher charging and discharging capacities and lower polarizations than those of NCM811/SiMP@PAA pouch cells (Fig. S50a). At higher charge and discharge capacities, the NCM811/SiMP@GG-g-PAA pouch cell exhibits significantly smaller thickness expansion and contraction than those of NCM811/SiMP@PAA pouch cell (Fig. S50b), strong confirming the superior role of the GG-g-PAA binder in suppressing the volume changes of the SiMP electrodes.

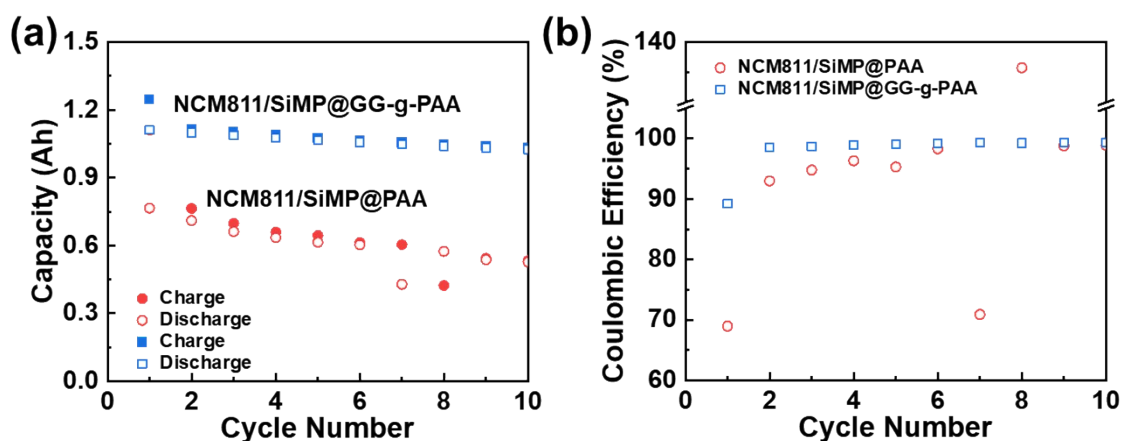


**Fig. S51** (a) Cycling performances and (b) corresponding CEs of the 6-layer parallel NCM811/SiMP@PAA and NCM811/SiMP@GG-g-PAA pouch cells at 0.1 C.

As shown in Fig. S51, a 6-layer parallel NCM811/SiMP@GG-g-PAA pouch cell exhibits excellent cycling stability. A discharge capacity of 1.02 Ah is left after 10 cycles at 0.1 C, which accounts for 92.2% of initial discharge capacity at 0.1 C. In contrast, the discharge capacity of a 6-layer parallel NCM811/SiMP@PAA pouch cell in the first cycle at 0.1 C is only 0.77 Ah, resulting in a low CE of 68.96%. Furthermore, the discharge capacity of the NCM811/SiMP@PAA pouch cell continues to decline and exhibits considerable fluctuations in subsequent cycles.

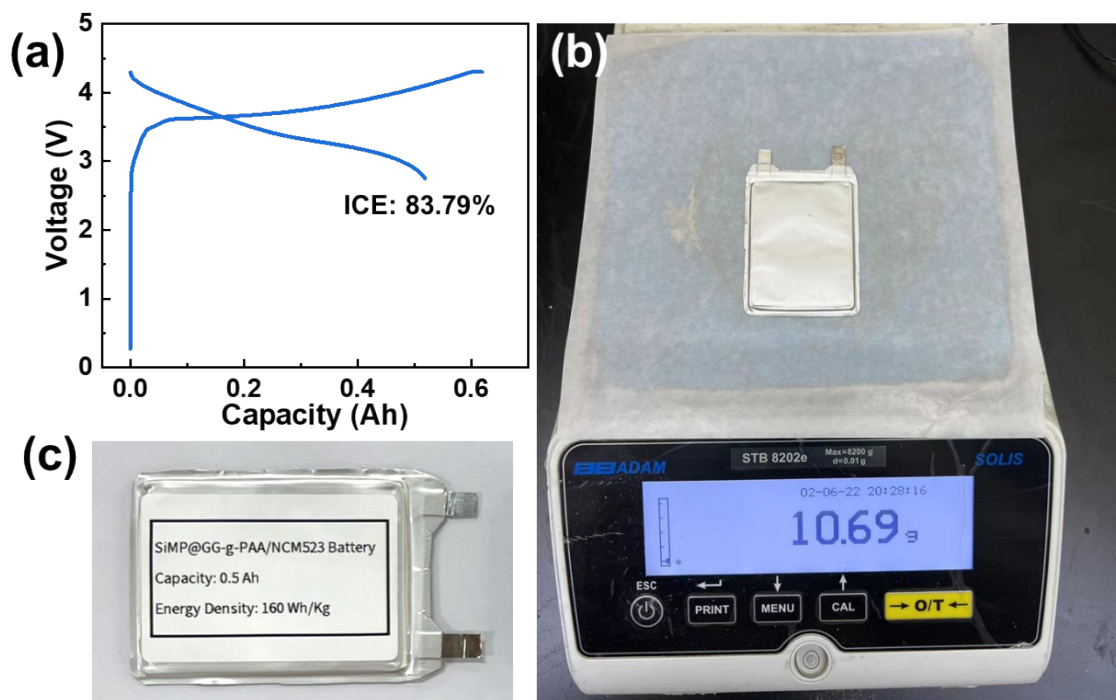


**Fig. S52** (a) Initial charge-discharge curves of the 0.5 Ah NCM523/SiMP@GG-g-PAA pouch cell when measured at 0.1 C. (b) The weight and (c) photograph of the 0.5 Ah NCM523/SiMP@GG-g-PAA pouch cell.

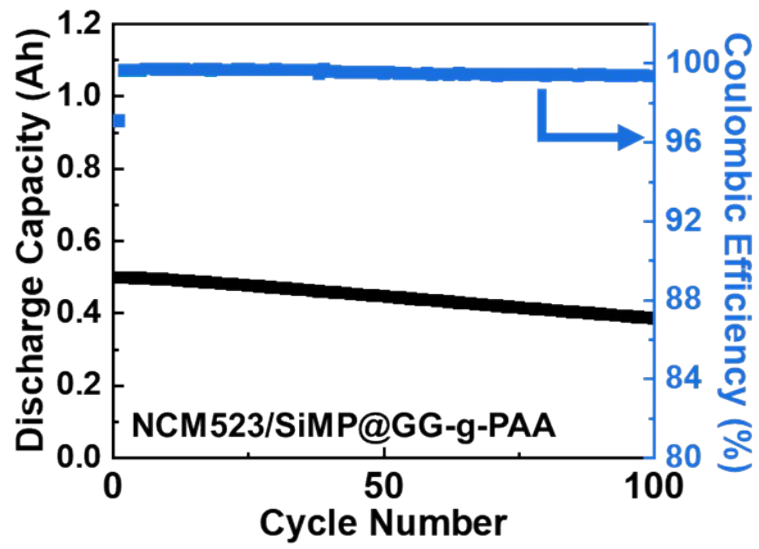


**Fig. S53** Cycling performance of the 0.5 Ah NCM523/SiMP@GG-g-PAA pouch cell at 0.2 C.

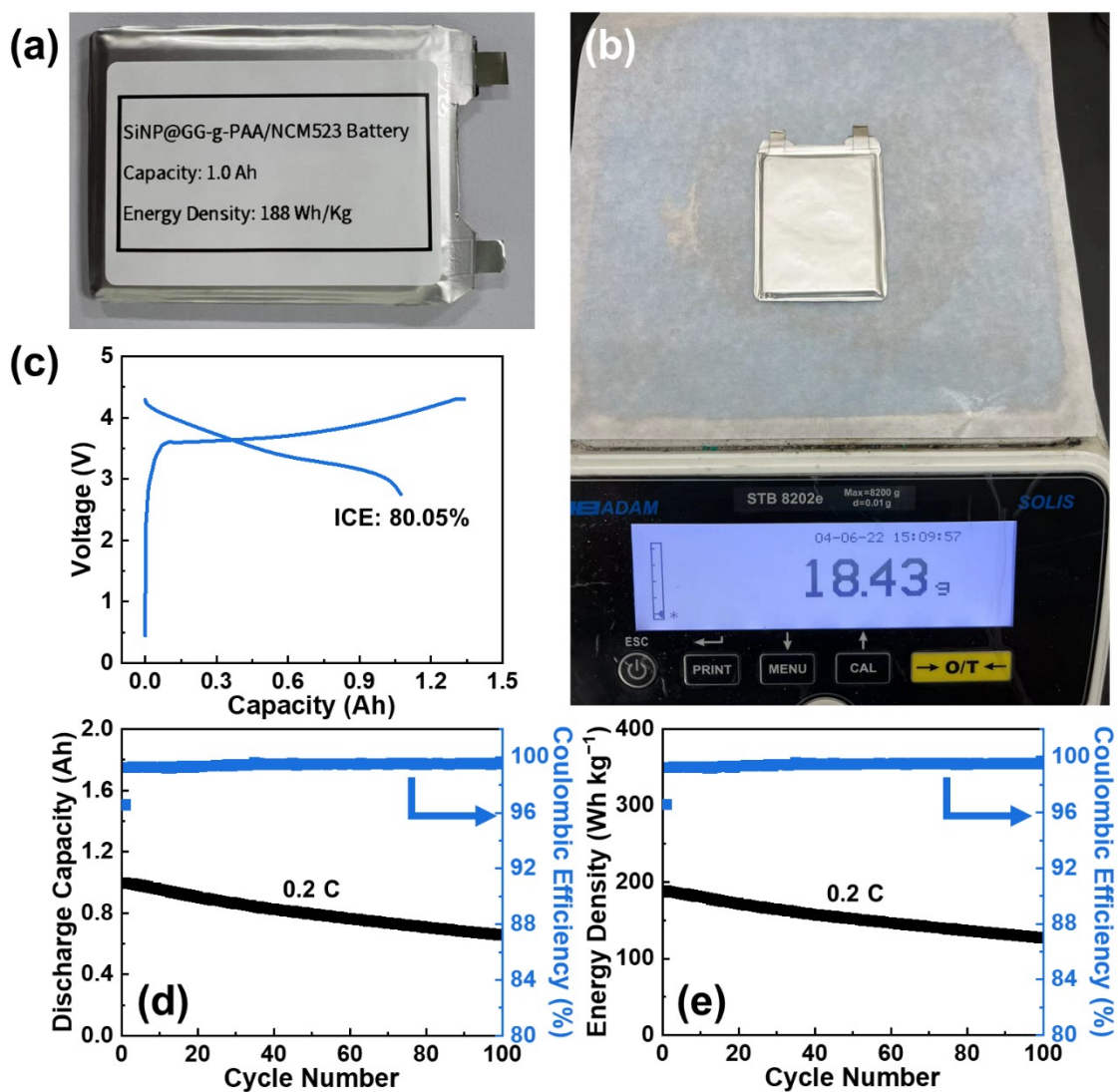


**Fig. S54** (a) The photograph and (b) weight of the 1.0 Ah NCM523/SiNP@GG-g-PAA pouch cell. (c) Initial charge-discharge curves of the 1.0 Ah NCM523/SiNP@GG-g-PAA pouch cell at 0.1 C. (d) The discharge capacity and (e) energy density of the 1.0 Ah NCM523/SiNP@GG-g-PAA pouch cell at 0.1 C.

The 1.0 Ah NCM523/SiNP@GG-g-PAA pouch cell exhibits a high ICE of 80.05% and maintains a capacity retention of ~70% after 100 cycles at 0.2 C with an average CE of 99.4%.

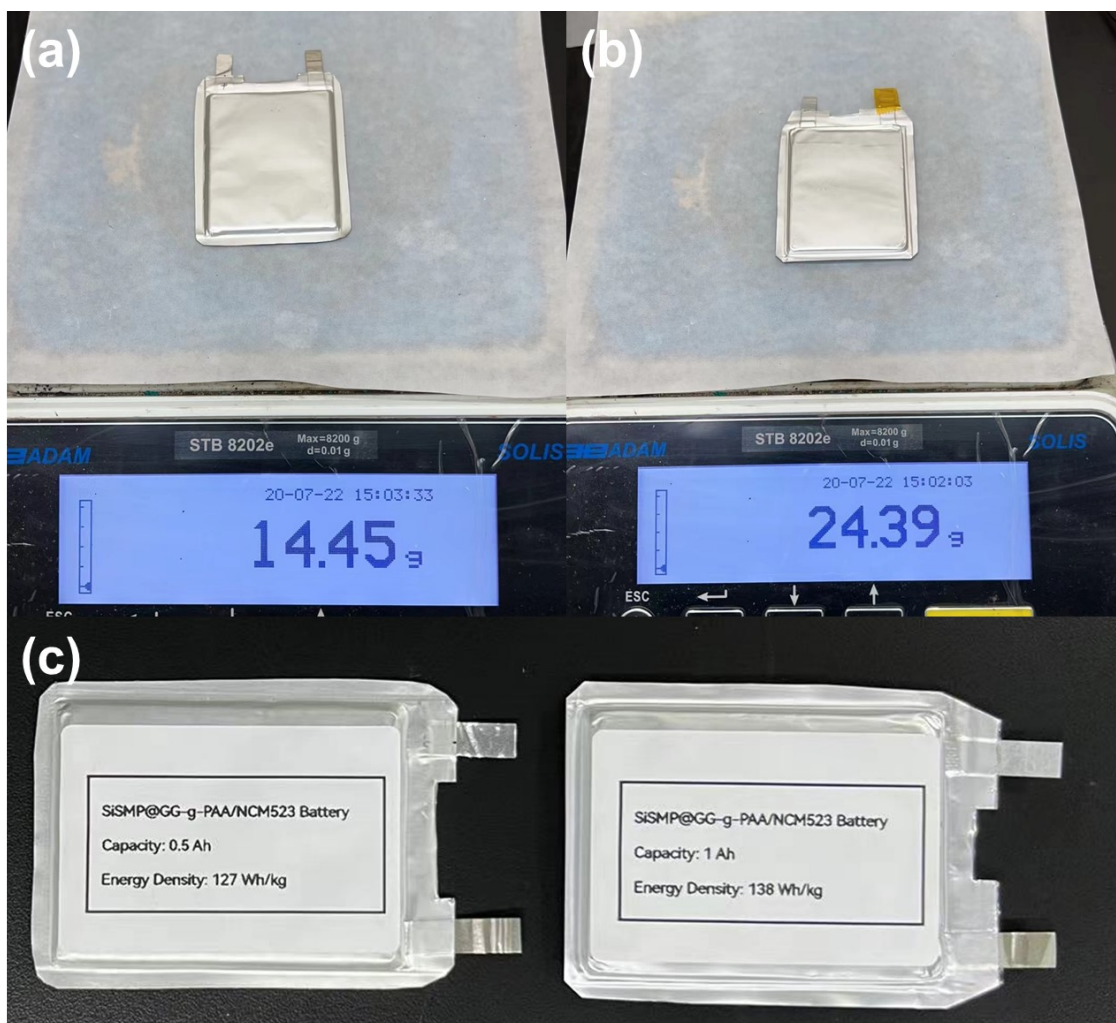


**Fig. S55** (a and b) The weights of the (a) 0.5 Ah and (b) 1.0 Ah NCM523/SiSMP@GG-g-PAA pouch cells. (c) The photograph of the 0.5 and 1.0 Ah NCM523/SiSMP@GG-g-PAA pouch cells.

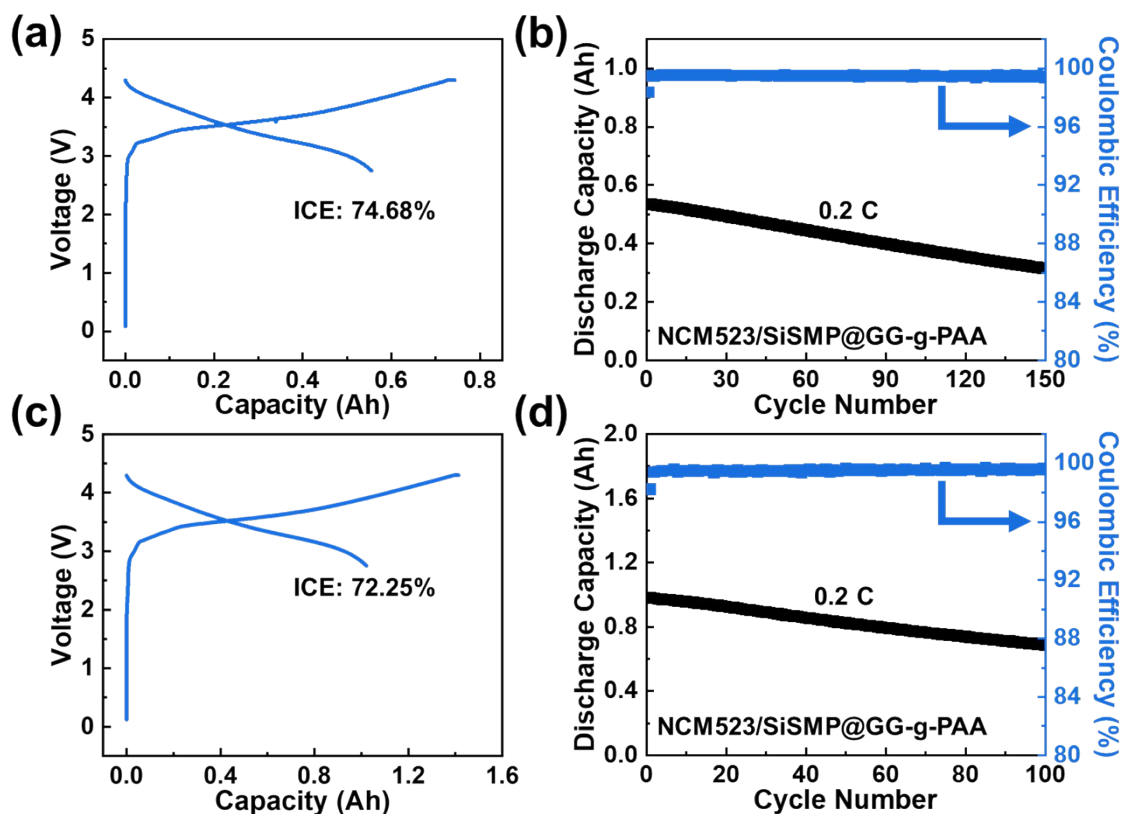


**Fig. S56** (a) Initial charge-discharge curves of the 0.5 Ah NCM523/SiSMP@GG-g-PAA pouch cell when measured at 0.1 C. (b) Cycling performance of the 0.5 Ah NCM523/SiSMP@GG-g-PAA pouch cell at 0.2 C. (c) Initial charge-discharge curves of the 1.0 Ah NCM523/SiSMP@GG-g-PAA pouch cell when measured at 0.1 C. (d) Cycling performance of the 1.0 Ah NCM523/SiSMP@GG-g-PAA pouch cell at 0.2 C.

Although the ICEs of NCM523/SiSMP@GG-g-PAA pouch cells are lower than the ICEs of NCM523/SiMP@GG-g-PAA and NCM523/SiNP@GG-g-PAA pouch cells, they exhibit similar cycle stability. The 0.5 Ah NCM523/SiSMP@GG-g-PAA pouch cell maintains a discharge capacity of 0.38 Ah with an average CE of 99.5% after 100 cycles at 0.2 C. The 1.0 Ah NCM523/SiSMP@GG-g-PAA pouch cell maintains a capacity retention over 70% with an average CE of 99.5% after 100 cycles at 0.2 C.

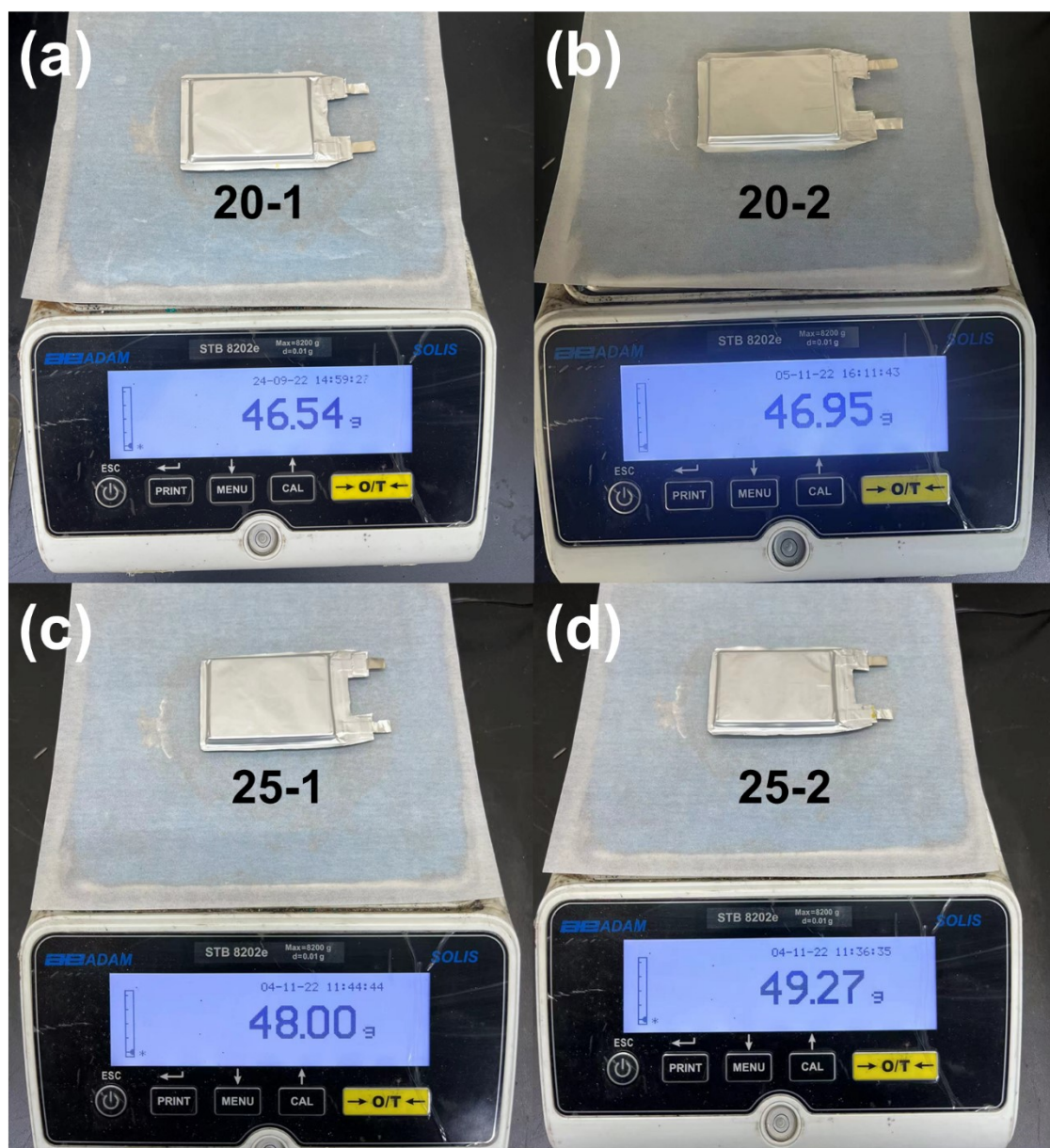


**Fig. S57** (a and b) The weights of two 20-layer NCM811/SiMP@GG-g-PAA pouch cells. (c and d) The weights of the two 25-layer NCM811/SiMP@GG-g-PAA pouch cells.

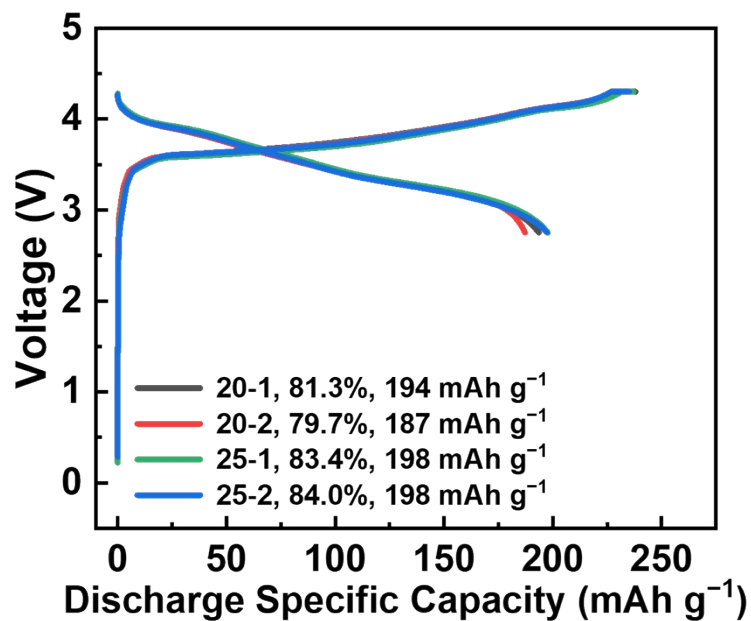


**Fig. S58** The specific capacities of the 20-layer and 25-layer NCM811/SiMP@GG-g-PAA pouch cells when measured at 0.05 C.

After the initial formation cycle at 0.05 C, all 20-layer and 25-layer NCM811/SiMP@GG-g-PAA pouch cells demonstrate a high discharge specific capacity. The 20-layer pouch cells achieve a capacity close to or exceeding  $190 \text{ mAh g}^{-1}$ , while the 25-layer pouch cells achieve very consistent capacities close to  $200 \text{ mAh g}^{-1}$  ( $198 \text{ mAh g}^{-1}$ ).

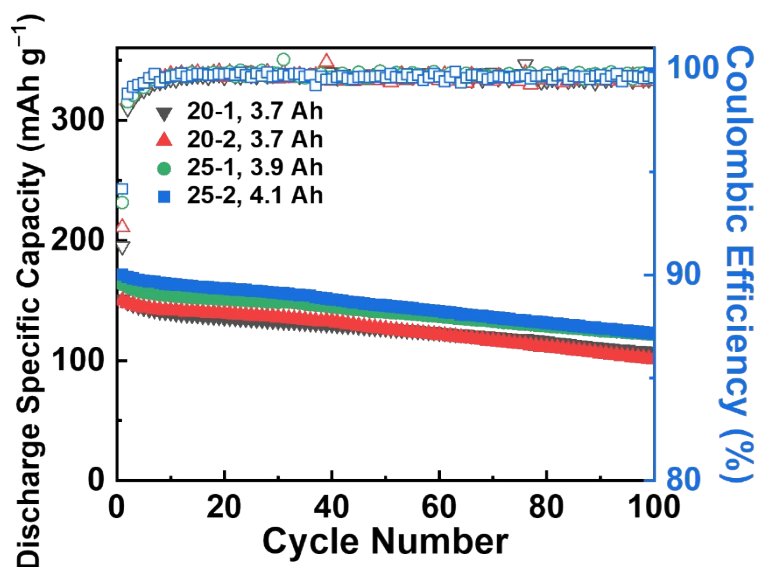


**Fig. S59** The discharge specific capacities of the 20-layer and 25-layer NCM811/SiMP@GG-g-PAA pouch cells when cycled at 0.2 C.

When cycled at 0.2 C, all 20-layer and 25-layer NCM811/SiMP@GG-g-PAA pouch cells achieve and maintain relatively high discharge specific capacities. Specially, two 25-layer pouch cells both exhibit a capacity close to or exceeding  $170 \text{ mAh g}^{-1}$  at the first cycle at 0.2 C, and after 100 cycles at 0.2 C, it remains greater than or equal to  $122 \text{ mAh g}^{-1}$ . These results strongly confirm the superior role of the GG-g-PAA in enhancing the interfacial chemistry/mechanical structural stability and Li-ion transport kinetics of high-loading SiMP anodes in practical pouch cells with high capacity and high energy density.

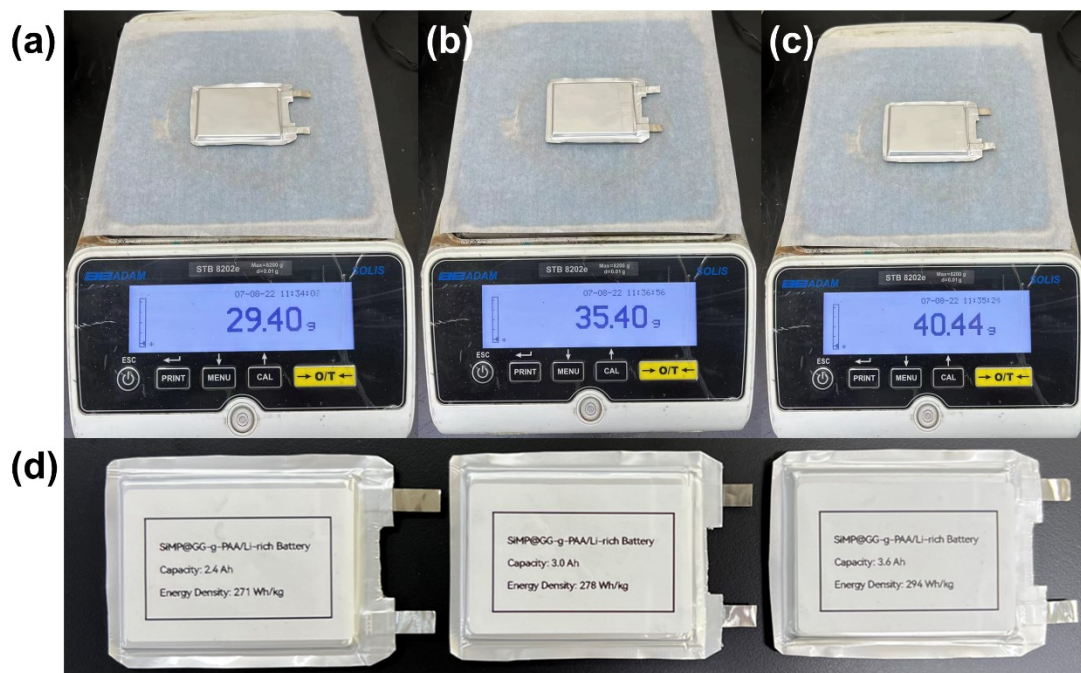


**Fig. S60** (a–c) The weights of (a) 2.4, (b) 3.0, and (c) 3.6 Ah Li-rich/SiMP@GG-g-PAA pouch cells. (d) The photograph of the 2.4, 3.0, and 3.6 Ah NCM811/SiMP@GG-g-PAA pouch cells.

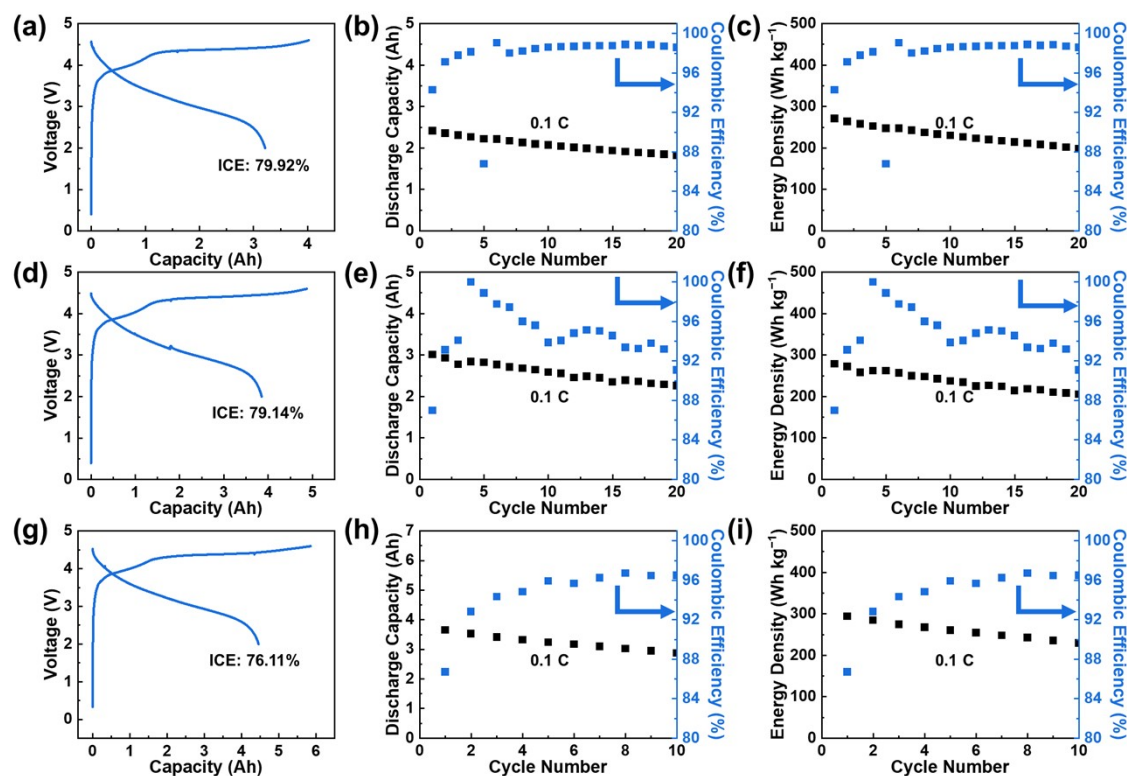


**Fig. S61** (a, d, and g) Initial charge-discharge curves of the (a) 2.4, (d) 3.0, and (g) 3.6 Ah Li-rich/SiMP@GG-g-PAA pouch cells when measured at 0.05 C. (b, e, and h) Discharge capacities of the (b) 2.4, (e) 3.0, and (h) 3.6 Ah Li-rich/SiMP@GG-g-PAA pouch cells at 0.1 C. (c, f, and i) Energy densities of the (c) 2.4, (f) 3.0, and (i) 3.6 Ah Li-rich/SiMP@GG-g-PAA pouch cells at 0.1 C.

**Table S1** The parameters for calculating Li-ion transference number of various binders.

<b>Binder</b>	$I_0$ ( $\mu\text{A}$ )	$I_s$ ( $\mu\text{A}$ )	$R_1^0$ (Ohm)	$R_1^s$ (Ohm)
<b>GG</b>	68.1	55.6	123.8	143.4
<b>PAA</b>	55.14	47.66	167.7	181.4
<b>GG-g-PAA</b>	60.8	46.3	127.1	151.8

**Table S2** Comparisons of electrochemical performances of SiMP@GG-g-PAA anodes with previous reported Si anodes using advanced binders at normal loadings.

Binders	Electrode Composition and ICE	Si Mass Loading $\text{mg cm}^{-2}$	Current Density $\text{A g}^{-1}$ (Based on the mass of Si)	Cycling Performance $\text{mAh g}^{-1}$ (normalized to active material)	Cycling Performance $\text{mAh g}^{-1}$ (normalized to total electrode)
<b>GG-g-PAA (This work)</b>	SiMPs: SP: binder = 80: 10: 10 Average ICE: 91.74%	0.6–1.1	2.1	2137 after 220 cycles, 91.2% CR from 21 <sup>th</sup> to 220 <sup>th</sup> cycle	1710 after 220 cycles
			4.2	1972 at 1 <sup>st</sup> cycle	1578 at 1 <sup>st</sup> cycle
				1610 at 10 <sup>th</sup> cycle	1288 at 10 <sup>th</sup> cycle
<b>PTBR<sup>16</sup></b>	SiMPs: SCNT-NH <sub>2</sub> : Binder = 70: 20: 10 ICE: 89.45%	0.6–1.1	2.0	1968 after 200 cycles, ~97% CR from 19 <sup>th</sup> to 200 <sup>th</sup> cycle	1968 after 200 cycles
			3.0	1719	1203
<b>PR-PAA<sup>17</sup></b>	SiMPs: SP: Binder = 80: 10: 10 ICE: 91.22%	1.0–1.1	0.6	2271 after 150 cycles, 91% CR	1817 after 150 cycles
			1.2	~1400 after 400 cycles (Li metal change)	~1120 after 400 cycles (Li metal change)
<b>AOB<sup>18</sup></b>	SiMPs: SP: Binder = 80:10:10	0.7	0.2 C	2767 after 100 cycles	2214 after 100 cycles
<b>PAA<sup>19</sup></b>	SiMPs: SCNT-NH <sub>2</sub> : Binder = 82.5: 7.5: 10 ICE: 89.7%	~1	1.2	1398 after 100 cycles	1398 after 100 cycles
			3	1471	1214
<b>PANa<sub>0.8</sub>Fe<sub>y</sub><sup>20</sup></b>	SiMPs: CB: Binder = 60: 20: 20 ICE: 92.3%	~1	1.8	~64% CR after 100 cycles	
			3.6	~1450	870

**Table S2** (continued)

<b>SHP-PEG<sup>21</sup></b>	SiMPs: CB: Binder = 65: 30: 5 ICE: ~83%	0.5–0.7	1.8	~1300 after 150 cycles 80% CR	~845 after 150 cycles
			3.6	~1400	~910
<b>SHP<sup>22</sup></b>	SiMPs: CB: Binder = 50: 6.5: 43.5 ICE: ~83%	0.5–0.7	0.4	2094 after 90 cycles, 80% CR	1047 after 90 cycles
<b>c-PTP-Alg<sup>23</sup></b>	SiMPs: CB: Binder = 70: 10: 20 ICE: 87.01%	0.5–0.7	0.8	80% CR from 2 <sup>nd</sup> to 80 <sup>th</sup> cycle	
			3.2	1430 at 1 <sup>st</sup> cycle	1001 at 1 <sup>st</sup> cycle
<b>PAA-5B<sup>24</sup></b>	SiMPs: AB: Binder = 60: 20: 20 ICE: 85.0%	1.2–1.5	0.5	91.2% CR from 2 <sup>nd</sup> to 80 <sup>th</sup> cycle	
			4	1320	792
<b>SHP<sup>25</sup></b>	SiMPs: CB: Binder = 63.5: 4.8: 31.7 ICE: 85.0%	0.75–1.1	0.36	1360 after 178 cycles 80% CR	1088 after 178 cycles
<b>PU-PDA<sup>26</sup></b>	SiMPs: SP: Binder = 60: 20: 20 ICE: 72.71%	0.75–1.1	0.2 C	1244 after 300 cycles 67% CR from 2 <sup>nd</sup> to 300 <sup>th</sup> cycle	746 after 300 cycles
<b>PAL-NaPAA<sup>27</sup></b>	SiMPs: SP: Binder = 60: 20: 20 ICE: 91.0%	0.7–0.8	0.84	1914 after 100 cycles	1148 after 100 cycles
<b>PAA-P(HEA- co-DMA)<sup>28</sup></b>	SiSMPs: SP: Binder = 80: 10: 10 ICE: 89.3%	~1	1	2394 after 220 cycles 93.8% CR from 2 <sup>nd</sup> to 220 <sup>th</sup> cycle	1915 after 220 cycles
			5	1855	1484
<b>ACC/PAA<sup>29</sup></b>	SiSMPs: SP: Binder = 80: 10: 10 ICE: 81.5%	1.0	0.6	1874 after 100 cycles 75% CR	1488 after 100 cycles
			2	1377	1102
<b>b-POD<sup>30</sup></b>	SiSMPs: C65: Binder: = 60: 20: 20 ICE: 89%	0.4–0.6	0.1 C	2277 after 100 cycles	1366 after 100 cycles

**Table S2** (continued)

<b>PG-c-ECH<sup>31</sup></b>	SiNPs: SP: Binder: = 80: 10: 10	0.4–0.6	2	2060 after 200 cycles, 88.8% CR from 2 <sup>nd</sup> to 200 <sup>th</sup> cycle	1648 after 200 cycles
<b>GG-g-PAM<sup>32</sup></b>	SiNPs: SP: Binder: = 80: 10: 10 ICE: 87.6%	0.8–1.0	1	2341 after 100 cycles, 83.9% CR	1873 after 100 cycles
<b>PAA- DA/PVA<sup>33</sup></b>	SiNPs: SP: Binder: = 60: 20: 20	/	0.4 4	73% CR after 100 cycles  2169	  1301
<b>PAA-BFPU<sup>34</sup></b>	SiNPs: SP: Binder: = 70: 15: 15 ICE: 89.75%	~1.0	2	88% CR after 200 cycles	/

**Table S3** Comparisons of electrochemical performances of SiMP@GG-g-PAA anodes with previous reported Si anodes using advanced binders at high loadings.

Binders	Electrode Composition and ICE	Si Mass Loading mg cm <sup>-2</sup>	Current Density A g <sup>-1</sup> (Based on the mass of Si)	Areal Capacity (mAh cm <sup>-2</sup> )
<b>GG-g-PAA (This work)</b>	SiMPs: SP: binder =80: 10: 10 Average ICE: 88.34%	1.6–2.1	0.42	4.2 after 50 cycles, CR: 77.4%
			0.84	2.4 for ~150 cycles (limited 1500 mAh g <sup>-1</sup> )
			0.74 mA cm <sup>-2</sup>	3.0 after 87 cycles
<b>PTBR<sup>16</sup></b>	SiMPs: SCNT-NH <sub>2</sub> : Binder = 70: 20: 10	1.4	0.6	3.6 after 50 cycles
		5.1	0.05 mA cm <sup>-2</sup>	20.6
<b>PAA<sup>19</sup></b>	SiMPs: SCNT-NH <sub>2</sub> : Binder = 82.5: 7.5: 10	5.37	0.6	19.37 at 1 <sup>st</sup> ~55% CR from 3 <sup>rd</sup> to 50 <sup>th</sup>
		14.12	0.1	40.27
<b>PAA-P(HEA-co-DMA)<sup>28</sup></b>	SiSMPs: SP: Binder = 80: 10: 10	1.74	0.5	over 4 for ~100 cycles
<b>PG-c-ECH<sup>31</sup></b>	SiNPs: SP: Binder: = 80: 10: 10 ICE: 81.6%	1.77	0.45	5.4 at 1 <sup>st</sup> 3.6 at 57 <sup>th</sup>
<b>GG-g-PAM<sup>32</sup></b>	SiNPs: SP: Binder: = 80: 10: 10 ICE: 84.6%	2.3	0.5	5.0 at 1 <sup>st</sup> 4.0 at 60 <sup>th</sup>
<b>SHA<sup>35</sup></b>	SiNPs: SP: Binder: = 60: 20: 20	2.6	0.5	4.2 at 1 <sup>st</sup> 1.7 at 60 <sup>th</sup>

**Table S3** (continued)

<b>PFA/PVA</b> <sup>36</sup>	SiNPs: SP: Binder: = 60: 20: 20	2.94	0.1	10 at 1 <sup>st</sup> 6 at 60 <sup>th</sup>
<b>SH-ECH</b> <sup>37</sup>	SiNPs: SP: Binder: = 70: 20: 10 ICE: 78.23%	3.0	0.42	12.4 at 1 <sup>st</sup> 4 at 50 <sup>th</sup>
<b>N-P-LiPN</b> <sup>38</sup>	SiNPs: SP: Binder: = 80: 10: 10 ICE: 82.89%	3.58 26.19	0.42 3.30 mA cm <sup>-2</sup>	9.23 at 1 <sup>st</sup> 5.58 at 35 <sup>th</sup> 49.59
<b>PAA-BFPU</b> <sup>34</sup>	SiNPs: SP: Binder: = 70: 15: 15	1.54	0.8	~2.6 after 100 cycles, 86% CR from 2 <sup>nd</sup> to 100 <sup>th</sup> cycle
<b>N-KCG-KG</b> <sup>39</sup>	SiNPs: SP: Binder: = 80: 10: 10 ICE: 76.78%	3.48	0.5	5.89 at 1 <sup>st</sup> 3.18 at 50 <sup>th</sup>

**Table S4** Comparisons of electrochemical performances of coin-type full cells based on Si anodes using advanced Si binders.

Binders	Cell Configuration and ICE	Electrode Composition	Current Rate	Areal Capacity (mAh cm <sup>-2</sup> ) and CR
<b>GG-g-PAA (This work)</b>	NCM811/SiMP@G G-g-PAA  Average ICE: 74.75%	Cathode: NCM811: SP: CNT: PVDF (NCM811: 94.5 wt%)  Anode: SiMPs: SP: binder = 80: 10: 10	0.2 C	Average: 2.7 after 50 cycles, 83%CR  Long term: 3.2 at 1 <sup>st</sup> , 2.4 at 100 <sup>th</sup> , 2.1 at 150 <sup>th</sup> , 1.8 at 200 <sup>th</sup>
<b>PTBR<sup>16</sup></b>	NCM811/pre-lithiated $\mu$ Si/PTBR	Cathode: NCM811:SP:PVDF = 80: 10: 10  Anode: SiMPs: SCNT-NH <sub>2</sub> : Binder = 70:20:10	0.1 C	1.85 after 50 cycles, 90.8% CR
<b>PR-PAA<sup>17</sup></b>	LiNi <sub>0.8</sub> Co <sub>0.15</sub> Al <sub>0.05</sub> O <sub>2</sub> (NCA)/PR-PAA-SiMP	Cathode: NCA:SP:PVDF = 90:5:5  Anode: SiMPs: SP: Binder = 80:10:10	0.2 C	~2.4 after 50 cycles, 98% CR
<b>PAA<sup>19</sup></b>	Li(Ni <sub>0.83</sub> Co <sub>0.07</sub> Mn <sub>0.10</sub> )O <sub>2</sub> (NCM)/ $\mu$ Si/SCNT-NH <sub>2</sub> -L ICE: 75%	Cathode: NCM:SP:PVDF = 80: 10: 10  Anode: SiMPs: SCNT-NH <sub>2</sub> : Binder = 82.5:7.5:10	0.1/0.2 C	1.89 after 5 cycles at 0.1 C and 45 cycles at 0.2 C, 75% CR
<b>c-PTP-Alg<sup>23</sup></b>	S-PAN/prelithiated SiMP@c-PTP-Alg	Cathode: S-PAN: SP: GG = 80: 10: 10  Anode: SiMPs: SP: Binder = 70:10:20	/	54.9% CR after 50 cycles

**Table S4** (continued)

<b>PU-PDA</b> <sup>26</sup>	LiFePO <sub>4</sub> (LFP)/prelithiated SiMP-PU-PDA	Cathode: LFP  Anode: SiMPs: SP: Binder = 60: 20: 20	/	1.1 after 50 cycles
<b>PAA-P(HEA-co-DMA)</b> <sup>28</sup>	LiNi <sub>1/3</sub> Co <sub>1/3</sub> Mn <sub>1/3</sub> O <sub>2</sub> (NCM111)/SiSMP- PAA-P(HEA-co- DMA)	Cathode: NCM111  Anode: SiSMPs: SP: Binder = 80: 10: 10	0.2 C	1.41 after 120 cycles, 80.8% CR
<b>AOB</b> <sup>18</sup>	NCM811/SiNP- AOB	Cathode: NCM811 (mass loading: 16 mg cm <sup>-2</sup> )  Anode: SiNPs: SP: Binder = 80: 10: 10	0.2 C	~2.4 after 200 cycles, ~80% CR
<b>PG-c-ECH</b> <sup>31</sup>	NCM523/SiNP@PG -c-ECH ICE: 55.2%	Cathode: NCM523:SP:PVDF = 90: 5: 5  Anode: SiNPs: SP: Binder = 80:10:10	0.1 C	1.56 after 60 cycles, 55% CR
<b>GG-g-PAM</b> <sup>32</sup>	NCM523 (NCM811)/SiNP@ GG-g-PAM	Cathode: NCM523(NMC811): SP: CNT : PVDF (NCM523: 94 wt%, NCM811: 94.5 wt%)  Anode: SiNPs: SP: Binder = 80: 10: 10	0.2 C	1.87 after 90 cycles, 73.6% CR (NCM523)  1.90 after 100 cycles, 66.7% CR (NCM811)
<b>N-KCG-KG</b> <sup>39</sup>	NCM523/SiNP@N- KCG-KG ICE: 72.0%	Cathode: NCM523: SP: PVDF=90: 6: 4  Anode: SiNPs: SP: Binder = 80: 10: 10	0.2 C	1.19 after 50 cycles. 54.1 % CR

The coin full cells assembled in this study show the highest active material content in the cathode, at 94.5 wt%, and the SiMP anode, at 80 wt%, surpassing that of previously reported pure Si anode-based coin full cells (Table S4). This active material content of the cathode notably exceeds the typical 80 wt% found in previous pure Si anode-based coin-type full cells. While reducing the active material content and increasing the concentration of binder and conductive additives can improve cycle stability, it is important to recognize that this adjustment significantly decreases the energy density of the cell. Typically, the practical cathode contains an active material content of approximately 94 wt%. Despite the high active material content, the coin full cells assembled in this study demonstrate stable cycling performance at commercially viable areal capacities.

**Table S5** Comparisons of electrochemical performances of pouch full cells based on Si anodes using advanced Si binders

Binders	Cell Configuration and ICE	Electrode Composition	Current Rate	Capacity (mAh) and average CE
<b>GG-g-PAA (This work)</b>	NCM811 (NCM523)/SiMP@ GG-g-PAA	Cathode: NCM811: SP: CNT: PVDF (NCM811: 94.5 wt%)	0.2 C	0.39 Ah at 100 <sup>th</sup> Average CE: 99.5 (NCM523)
	ICE: 83.79% (NCM523) Average ICE: 80.51% (20-layer NCM811) 83.70% (25-layer NCM811)	NCM523: SP: CNT: PVDF = 94:2:2:2  Anode: SiMPs: SP: binder = 80:10:10	0.1 C	Average: 2.56 Ah at 100 <sup>th</sup> , Average CE: 99.5% (20-layer NCM811) Average: 2.95 Ah at 100 <sup>th</sup> , Average CE: 99.6% (25-layer NCM811)
<b>PFA/PVA</b> <sup>36</sup>	Li-rich/SiNP- PFA/PVA  ICE: 47.9%	Cathode: Li-rich Mn-based  Anode: SiNPs: SP: Binder = 60: 20: 10	0.5 C	~500 mAh at 35 <sup>th</sup> Average CE: 92%
<b>GG-g-PAM</b> <sup>32</sup>	NCM523/Si@GG- G-PAM  ICE: 81.0%	Cathode: NCM523: SP: CNT: PVDF = 94:2:2:2  Anode: SiNPs: SP: Binder = 80: 10: 10	0.2 C	0.5-Ah pouch cell: 351.1 mAh at 100 <sup>th</sup> Average CE: 99.0%  1.1-Ah pouch cell 809.5 mAh at 70 <sup>th</sup> Average CE: 99.1%
<b>N-P-LiPN</b> <sup>38</sup>	NCM523/SiNP@N- P-LiPN  ICE: 71.5%	Cathode: NCM523: SP: PVDF = 80: 10: 10  Anode: SiNPs: SP: Binder = 80: 10: 10	0.2 C	29.1 mAh at 140 <sup>th</sup> Average CE: 99.4%
<b>PG-c-ECH</b> <sup>31</sup>	NCM523/SiNP@PG -c-ECH  ICE: 64.4%	Cathode: NCM523: SP: PVDF= 90: 5: 5  Si:SP:Binder = 75: 10: 15	0.1 C	11.1 mAh at 100 <sup>th</sup> Average CE: 99.0%

## Reference

- 1 W. Zeng, L. Wang, X. Peng, T. Liu, Y. Jiang, F. Qin, L. Hu, P. K. Chu, K. Huo, Y. Zhou, *Adv. Energy Mater.*, 2018, **8**, 1702314.
- 2 R. Xu, X. Q. Zhang, X. B. Cheng, H. J. Peng, C. Z. Zhao, C. Yan and J. Q. Huang, *Adv. Funct. Mater.*, 2018, **28**, 1705838.
- 3 Z. Wu, Z. Wan, Z. Li, Q. Du, T. Wu, J. Cao, M. Ling, C. Liang and Y. Tan, *Small*, 2023, **19**, 2205065.
- 4 G. Kresse and J. Furthmüller, *Phy. Rev. B*, 1996, **54**, 11169.
- 5 J. P. Perdew, K. Burke and M. Ernzerhof, *Phy. Rev. Lett.*, 1996, **77**, 3865.
- 6 G. Kresse and D. Joubert, *Phy. Rev. B*, 1999, **59**, 1758.
- 7 P. E. Blöchl, *Phy. Rev. B*, 1994, **50**, 17953.
- 8 K. Momma and F. Izumi, *J. Appl. Crystallogr.*, 2011, **44**, 1272–1276.
- 9 S. Grimme, S. Ehrlich and L. Goerigk, *J. Comput. Chem.*, 2011, **32**, 1456–1465.
- 10 X. H. Liu, L. Zhong, S. Huang, S. X. Mao, T. Zhu and J. Y. Huang, *ACS Nano*, 2012, **6**, 1522–1531.
- 11 T.-w. Kwon, J. W. Choi and A. Coskun, *Chem. Soc. Rev.*, 2018, **47**, 2145–2164.
- 12 J. Liu, Q. Zhang, T. Zhang, J. T. Li, L. Huang and S. G. Sun, *Adv. Funct. Mater.*, 2015, **25**, 3599–3605.
- 13 S. Guo, H. Li, Y. Li, Y. Han, K. Chen, G. Xu, Y. Zhu and X. Hu, *Adv. Energy Mater.*, 2018, **8**, 1800434.
- 14 Z. Cao, X. Zheng, Q. Qu, Y. Huang and H. Zheng, *Adv. Mater.*, 2021, **33**, 2103178.
- 15 S. K. Heiskanen, J. Kim and B. L. Lucht, *Joule*, 2019, **3**, 2322–2333.
- 16 B. Zhang, Y. Dong, J. Han, Y. Zhen, C. Hu and D. Liu, *Advanced Materials*, 2023, **35**, 2301320.
- 17 S. Choi, T.-w. Kwon, A. Coskun and J. W. Choi, *Science*, 2017, **357**, 279–283.
- 18 P. Mu, S. Zhang, H. Zhang, J. Li, Z. Liu, S. Dong and G. Cui, *Adv. Mater.*, 2023, **35**, 2303312.
- 19 B. Zhang, D. Liu, H. Xie, D. Wang, C. Hu and L. Dai, *J. Power Sources*, 2022, **539**, 231591.
- 20 H. Woo, B. Gil, J. Kim, K. Park, A. J. Yun, J. Kim, S. Nam and B. Park, *Batteries Supercaps*, 2020, **3**, 1287–1295.
- 21 T. Munaoka, X. Yan, J. Lopez, J. W. To, J. Park, J. B. H. Tok, Y. Cui and Z. Bao, *Adv. Energy Mater.*, 2018, **8**, 1703138.
- 22 C. Wang, H. Wu, Z. Chen, M. T. McDowell, Y. Cui and Z. Bao, *Nat. Chem.*, 2013, **5**, 1042–1048.
- 23 J. Feng, M. Hou, Q. Zhang, D. Wang, Z. Li, J. Liu, Y. Wu and L. Wang, *J. Colloid Interf. Sci.*, 2023, **634**, 621–629.
- 24 S. Wang, Q. Duan, J. Lei and Y. Denis, *J. Power Sources*, 2020, **468**, 228365.
- 25 J. Lopez, Z. Chen, C. Wang, S. C. Andrews, Y. Cui and Z. Bao, *ACS Appl. Mater. Interfaces*, 2016, **8**, 2318–2324.
- 26 L. Ma, S. Niu, F. Zhao, R. Tang, Y. Zhang, W. Su, L. Wei, G. Tang, Y. Wang and A. Pang, *ACS Appl. Energy Mater.*, 2022, **5**, 7571–7581.
- 27 C. Luo, L. Du, W. Wu, H. Xu, G. Zhang, S. Li, C. Wang, Z. Lu and Y. Deng, *ACS Sustain. Chem. Eng.*, 2018, **6**, 12621–12629.

- 28 Z. Xu, J. Yang, T. Zhang, Y. Nuli, J. Wang and S.-i. Hirano, *Joule*, 2018, **2**, 950–961.
- 29 M. Tian, X. Chen, S. Sun, D. Yang and P. Wu, *Nano Res.*, 2019, **12**, 1121–1127.
- 30 Y. Yu, J. Zhu, K. Zeng and M. Jiang, *J. Mater. Chem. A*, 2021, **9**, 3472–3481.
- 31 Z. Li, Z. Wan, X. Zeng, S. Zhang, L. Yan, J. Ji, H. Wang, Q. Ma, T. Liu and Z. Lin, *Nano Energy*, 2021, **79**, 105430.
- 32 Z. Li, G. Wu, Y. Yang, Z. Wan, X. Zeng, L. Yan, S. Wu, M. Ling, C. Liang and K. N. Hui, *Adv. Energy Mater.*, 2022, **12**, 2201197.
- 33 X. Wan, C. Kang, T. Mu, J. Zhu, P. Zuo, C. Du and G. Yin, *ACS Energy Lett.*, 2022, **7**, 3572–3580.
- 34 X. X. Jiao, J. Q. Yin, X. Y. Xu, J. L. Wang, Y. Y. Liu, S. Z. Xiong, Q. L. Zhang and J. X. Song, *Adv. Funct. Mater.*, 2021, **31**, 2005699.
- 35 Y. Li, B. Jin, K. Wang, L. Song, L. Ren, Y. Hou, X. Gao, X. Zhan and Q. Zhang, *Chem. Eng. J.*, 2022, **429**, 132235.
- 36 T. Liu, Q. Chu, C. Yan, S. Zhang, Z. Lin and J. Lu, *Adv. Energy Mater.*, 2019, **9**, 1802645.
- 37 H. X. Wang, D. Wei, B. Zhang, Z. K. Ji, L. G. Wang, M. Ling and C. D. Liang, *ACS Appl. Mater. Interfaces*, 2021, **13**, 37704–37712.
- 38 Z. Li, Y. Zhang, T. Liu, X. Gao, S. Li, M. Ling, C. Liang, J. Zheng and Z. Lin, *Adv. Energy Mater.*, 2020, **10**, 1903110.
- 39 Z. Li, Z. Wan, G. Wu, Z. Wu, X. Zeng, L. Gan, J. Liu, S. Wu, Z. Lin and X. Gao, *Sustain. Mater. Techno.*, 2021, **30**, e00333.